International Journal of Non-Linear Mechanics 148 (2023) 104291

Contents lists available at ScienceDirect

International Journal of Non-Linear Mechanics

journal homepage: www.elsevier.com/locate/nlm

A strong-form meshfree collocation method for modeling stationary cracks with frictional contact

Ashkan Almasi [a], Young-Cheol Yoon [b], Tae-Yeon Kim [c], Tod A. Laursen [d], Jeong-Hoon Song [a,*,1]

[a] Department of Civil, Environmental and Architectural Engineering, University of Colorado, Boulder, CO 80309, USA
[b] Department of Civil Engineering, Myongji College, Seoul 120-776, South Korea
[c] Civil Infrastructure and Environmental Engineering, Khalifa University of Science and Technology, Abu Dhabi, 127788, United Arab Emirates
[d] SUNY Polytechnic Institute, 100 Seymour Road, Utica, NY 13502, USA

ARTICLE INFO

Keywords:
Strong form
Meshfree
Point collocation
Multi-body contact
Frictional crack

ABSTRACT

We present a strong-form meshfree collocation method for frictional contact of two deformable bodies within the context of frictional crack problems. The method inherently achieves desirable features of meshfree methods by completely avoiding the construction of meshes or grids, such that the only required numerical approximation units are nodes (used as collocation points). For the recognition of a contact or crack surface, a line segment is used without any connection with the node structure. A contact constraint due to two body frictional contact is implemented in the strong-form meshfree discretization. Since the contact boundary is a Neumann boundary, it contributes to the system of equations as a traction boundary condition, but it does not yield extra unknowns. Although the material is linear elastic, the presence of the constraint formulation leads to an iterative nonlinear solution procedure. The assembled discrete system generates a consistent and stable solution despite the presence of contact constraints and the crack discontinuity, because the constraint formulation and crack modeling are well combined with the strong-form meshfree collocation method. Numerical experiments demonstrate the robustness and consistency of the method through comparison with analytical and finite element solutions.

1. Introduction

Meshfree methods have an advantage in modeling various types of discontinuity problems because they apparently do not require a mesh. However, weakly formulated meshfree methods such as the element-free Galerkin method (EFGM) [1] and the reproducing kernel particle method (RKPM) [2] cannot avoid a so called integration cell. Although the integration cell does not need the connectivity, it still demands some sort of cell structures which may prove cumbersome process in discontinuity modeling. Discontinuity modeling schemes such as the visibility criterion [3,4] and intrinsic or extrinsic near-tip field enrichments [4] might circumvent further sub-division of the integration cell from the weak formulation for crack problems, but they do not completely remove inconvenience arising from the requirement of a cell structure.

To fully take advantage of the merit of meshless methods without the need for integration cells, strong-form based meshfree methods [5,6] have been proposed, with their own approaches to deal with the collocation scheme and derivative approximation techniques. Among them, Aluru [6] proposed a meshfree collocation method based on reproducing kernel approximations for solid mechanics problems, obtaining the second-order derivative approximation by directly differentiating the zeroth-order approximation. The strong-form based meshfree collocation method adopted in this study [7–9] has been used for crack analysis [10], weak discontinuity analysis [11], phase field simulation of microstructure solidification problems [12,13], and thermo-mechanical contact problems [14]. Motivated by such successful applications, we propose here a further extension of the strong-form based collocation method to model arbitrary stationary cracks with frictional contact on the crack surfaces.

For crack modeling, the strong-form meshfree collocation method has its own distinct advantages. The main advantage of the method is an easy adaptive nodal refinement near the tip region and contact area. More specifically, when there is no intrinsic or extrinsic function enrichments for the near tip field, the node refinement is essential for the accurate stress analysis. This may apply to the contact problems in the same way. Furthermore, the introduction of contact constraint does not increase the size of the final system, not because extra unknowns are created, but because Neumann boundary conditions are added by contact surfaces (note that contact constraint is naturally treated as a traction boundary). Another advantage is an easy and fast construction of the high-order derivative approximation based on the Tayler

* Corresponding author.
E-mail address: jh.song@colorado.edu (J.-H. Song).
[1] Associate Professor.

https://doi.org/10.1016/j.ijnonlinmec.2022.104291
Received 27 April 2022; Received in revised form 6 October 2022; Accepted 21 October 2022
Available online 28 October 2022
0020-7462/

expansion using the moving least squares approximation. Because crack problems usually require the second-order derivative of a variable function, an efficient high-order derivative approximation is inevitable for discretizing the governing equations and is easily introduced through the approach we propose. Moreover, the visibility criterion for crack analysis can be easily combined with the fast derivative approximation.

Upon making use of such advantages, Lee et al. [15] successfully applied the strong-form meshfree collocation method to dynamic crack propagations. The hybrid time integrators, based on the central difference and Newmark schemes, were used to effectively eliminate oscillation occurred during the time marching fracture simulation. Yoon et al. [16] analyzed dynamic fracture of a concrete beam. The Rayleigh damping effect was incorporated into the strong-form meshfree collocation method via the proportional damping algorithm to model the dissipation of the driving force for dynamic fracture. More recently, concrete tensile failure subjected to strain-rate effects was successfully simulated by Kim et al. [17]. The proportional damping algorithm, damage model and visibility criterion were combined together for the simulation of the extremely high loading rate fracture in the framework of the strong-form meshfree collocation method. In particular, an order reduced strong formulation was developed to employ material models including a damage model for local concrete failure. Rabczuk et al. [18] summarized approaches of modeling cracks in other meshfree methods. Furthermore, they introduced a robust and efficient approach for modeling discrete cracks using a set of cracked segments and the visibility method motivated by the cracking particle method [19] where the crack can be modeled by a discontinuous enrichment that can be arbitrarily aligned in the body at each node.

Several collocation based numerical methods have been dealt with contact problems. Examples include the isogeometric analysis collocation method and non-conventional numerical schemes using the kernel function [20,21]. The isogeometric analysis collocation method, which is not the strong-form based meshfree method, studied frictionless and frictional contact problems for an elastic body [22,23] and a rod-to-rod contact [24]. Recently, Almasi et al. [25] successfully applied the strong-form meshfree collocation method to one-body frictional contact problems. Motivated by this, this study focuses on further extension of the strong-form meshfree collocation method to the contact between two deformable bodies including a frictional crack. The crack is treated as a strong discontinuity with a stress singularity before any contact occurs at the crack surface, but it is handled as a contact interface after contact. A constitutive equation for the contact surface is given by contact kinematics and a penalty algorithm is implemented in an explicit manner. Notice that the contact surface differs from the material interface which does not allow any sliding. This study shows how the contact constraint is effectively implemented in the strong-form meshfree collocation formulation by using the penalty method without yielding any extra unknowns along the interface. Although the developed method generates the additional residual equations, it preserves the nodal displacements as one and only category of unknown variable to be determined from solving the global system of equations. The stiffness matrix of the global system will be shown to be effective in the nonlinear iterative solution process through numerical experiments.

The outline of the paper is organized as follows. In Section 2, we explain the fast particle derivative approximation which is optimized for the strong-form meshfree collocation method. In Section 3, the strong-form based contact formulation is presented for deformable multi-body contact problems. In Section 4, numerical verification for the proposed collocation method is performed for two-body frictional contact and frictional crack problems. In Section 5, a summary is provided with concluding remarks.

2. Particle derivative approximation

For the strong-form based discretization, the high-order derivative approximation is crucial because the governing equation is mostly given in the partial differential equation with high order. For instance, the momentum equation for the solid mechanics problems involves the second order derivative functions while the natural boundary condition is the first order derivative function. The strong-form meshfree collocation method allows a non-exact form of the derivative approximation in a mathematical sense. In the weak formulation, the derivative approximation is implemented in the integral calculation with an average sense due to numerical integration process but it is required to be mathematically exact. However, in the strong formulation, it needs to satisfy the reproducing property or consistency condition in a sense of Taylor theorem, but it does not have to be mathematically exact. It was already proved that the particle derivative approximation achieves sufficient accuracy and efficiency for the strong form based meshfree methods [7,8]. The weak formulation obtains the derivative approximation by directly differentiating the approximation function. However, the particle derivative approximation is derived from the Taylor series expanded by the moving least squares method without any differentiation process. As a result, no extra effort is taken to get the derivative approximation. The strong-form meshfree collocation method employs the particle derivative approximation instead of the exact derivative of the moving least squares approximation. It implies that the Taylor polynomial is able to approximate the given function or the solution of the governing equation. Note that differentiation of the moving least squares approximation is quite complicated and the approximate derivative like the particle derivative approximation can be used in the strong formulation as long as it achieves the reproducing property or consistency condition [7–9].

The details of the moving least squares approximation and their derivatives can be found in [7–9]. Here, we provide the brief derivation of the derivative approximation. The Taylor polynomial expanded with the moving least squares approximation can approximate the derivatives of the field variable up to the order of consistency. For convenience, we start by defining some useful mathematical notations. Let $\mathbf{x} = (x_1, \dots, x_n)$ be an n-dimensional real vector and $\boldsymbol{\alpha} = (\alpha_1, \dots, \alpha_n)$ be an n-tuple of non-negative integers for power and derivative of a vector. The $\boldsymbol{\alpha}$th power of $\mathbf{x}$ is defined by $\mathbf{x}^{\boldsymbol{\alpha}} = x_1^{\alpha_1} x_2^{\alpha_2} \cdots x_n^{\alpha_n}$. We define the $\boldsymbol{\alpha}$th derivative of a smooth function $f(\mathbf{x})$ with respect to $\mathbf{x}$ as

$$D_{\mathbf{x}}^{\boldsymbol{\alpha}} f(\mathbf{x}) = \frac{\partial^{|\boldsymbol{\alpha}|} f(\mathbf{x})}{\partial x_1^{\alpha_1} \partial x_2^{\alpha_2} \cdots \partial x_n^{\alpha_n}} \tag{2.1}$$

where $|\boldsymbol{\alpha}|$ is the sum of all components of $\boldsymbol{\alpha}$, i.e., $|\boldsymbol{\alpha}| \equiv \sum_{i=1}^{n} \alpha_i$.

Upon neglecting higher-order terms in a Taylor series, the mth-order polynomial for approximating a continuous function $u(\mathbf{x})$ at the local center $\bar{\mathbf{x}}$ can be expressed as

$$u(\mathbf{x}; \bar{\mathbf{x}}) = \sum_{|\boldsymbol{\alpha}| \le m} \frac{(\mathbf{x} - \bar{\mathbf{x}})^{\boldsymbol{\alpha}}}{\boldsymbol{\alpha}!} D_{\mathbf{x}}^{\boldsymbol{\alpha}} u(\bar{\mathbf{x}}) = \mathbf{p}_m^{\top}(\mathbf{x}; \bar{\mathbf{x}}) \mathbf{a}(\bar{\mathbf{x}}) \tag{2.2}$$

where $\boldsymbol{\alpha}!$ is the factorial of $\boldsymbol{\alpha}$, i.e., $\boldsymbol{\alpha}! = \alpha_1! \cdots \alpha_n!$. Note that the Taylor polynomial can be decomposed into the polynomial basis vector $\mathbf{p}_m^{\top}(\mathbf{x}; \bar{\mathbf{x}})$ and the corresponding derivative coefficient vector $\mathbf{a}(\bar{\mathbf{x}})$ computed at $\bar{\mathbf{x}}$ the local center. From the definition of the Taylor polynomial, the polynomial basis vector takes the form

$$\mathbf{p}_m^{\top}(\mathbf{x}; \bar{\mathbf{x}}) = \left[\frac{(\mathbf{x} - \bar{\mathbf{x}})^{\boldsymbol{\alpha}_1}}{\boldsymbol{\alpha}_1!}, \dots, \frac{(\mathbf{x} - \bar{\mathbf{x}})^{\boldsymbol{\alpha}_L}}{\boldsymbol{\alpha}_L!} \right] \tag{2.3}$$

where $L = (n + m)!/n!m!$ is the number of the components of the polynomial basis vector $\mathbf{p}_m^{\top}$ and $(\mathbf{x} - \bar{\mathbf{x}})^{\boldsymbol{\alpha}_i}$ is the $\boldsymbol{\alpha}_i$th-power of $\mathbf{x} - \bar{\mathbf{x}}$ defined by $(\mathbf{x} - \bar{\mathbf{x}})^{\boldsymbol{\alpha}_i} = (x_1 - \bar{x}_1)^{\alpha_1} (x_2 - \bar{x}_2)^{\alpha_2} \cdots (x_n - \bar{x}_n)^{\alpha_L}$. The derivative coefficient vector can be written as

$$\mathbf{a}^{\top}(\bar{\mathbf{x}}) = \left[D_{\mathbf{x}}^{\boldsymbol{\alpha}_1} u(\bar{\mathbf{x}}), \dots, D_{\mathbf{x}}^{\boldsymbol{\alpha}_L} u(\bar{\mathbf{x}}) \right] \tag{2.4}$$

which includes all of the derivatives for $u(\mathbf{x})$ at $\bar{\mathbf{x}}$ up to the $\boldsymbol{\alpha}_L$th-order.

Based on the idea of moving least-square approximation, minimizing with respect to $\mathbf{a}(\bar{\mathbf{x}})$ the discrete form of the weighted discrete L^2-norm given by

$$\mathbf{J} = \sum_{I=1}^{N} w \left(\frac{\mathbf{x}_I - \bar{\mathbf{x}}}{\rho_{\bar{\mathbf{x}}}} \right) [\mathbf{p}^{\top}(\mathbf{x}_I; \bar{\mathbf{x}}) \mathbf{a}(\bar{\mathbf{x}}) - u_I]^2 \tag{2.5}$$

yields

$$\mathbf{a}(\bar{\mathbf{x}}) = \mathbf{M}^{-1}(\bar{\mathbf{x}})\mathbf{B}(\bar{\mathbf{x}})\mathbf{u} \tag{2.6}$$

where $u_I = u(\mathbf{x}_I)$ and $\mathbf{u}^\top = \left[u_1, u_2, \dots, u_N\right]$. The matrices $\mathbf{M}$ and $\mathbf{B}$ are defined by

$$\mathbf{M}(\bar{\mathbf{x}}) = \sum_{I=1}^{N} w\left(\frac{\mathbf{x}_I - \bar{\mathbf{x}}}{\rho_{\bar{\mathbf{x}}}}\right)\mathbf{p}_m(\mathbf{x}_I;\bar{\mathbf{x}})\mathbf{p}_m^\top(\mathbf{x}_I;\bar{\mathbf{x}}), \tag{2.7}$$

$$\mathbf{B}(\bar{\mathbf{x}}) = \left[w\left(\frac{\mathbf{x}_1-\bar{\mathbf{x}}}{\rho_{\bar{\mathbf{x}}}}\right)\mathbf{p}_m(\mathbf{x}_1;\bar{\mathbf{x}}), \quad \cdots, \quad w\left(\frac{\mathbf{x}_N-\bar{\mathbf{x}}}{\rho_{\bar{\mathbf{x}}}}\right)\mathbf{p}_m(\mathbf{x}_N;\bar{\mathbf{x}})\right] \tag{2.8}$$

where $w\left(\frac{\mathbf{x}_I-\bar{\mathbf{x}}}{\rho_{\bar{\mathbf{x}}}}\right)$ indicates the weight function with support size $\rho_{\bar{\mathbf{x}}}$. In Eq. (2.6), substituting $\mathbf{x}$ for $\bar{\mathbf{x}}$ gives the particle derivative approximation at an arbitrary position $\mathbf{x}$; the constitution of $\mathbf{a}(\mathbf{x})$ can be noted from Eq. (2.2). The derivative approximation is combined with the generalized nodal shape function and nodal solution as follows

$$\mathbf{D}_{\mathbf{x}}^{\boldsymbol{\alpha}} u(\mathbf{x}) = \sum_{I=1}^{N} \boldsymbol{\Phi}_I^{\boldsymbol{\alpha}}(\mathbf{x}) u_I \tag{2.9}$$

where $\boldsymbol{\alpha}$ is a 2-tuple of non-negative integers for 2D case. Eq. (2.9) can be rewritten in matrix form as following

$$\begin{pmatrix} \mathbf{D}_{\mathbf{x}}^{\boldsymbol{\alpha}_1} u(\mathbf{x}) \\ \mathbf{D}_{\mathbf{x}}^{\boldsymbol{\alpha}_2} u(\mathbf{x}) \\ \vdots \\ \mathbf{D}_{\mathbf{x}}^{\boldsymbol{\alpha}_L} u(\mathbf{x}) \end{pmatrix} = \begin{pmatrix} \boldsymbol{\Phi}_1^{\boldsymbol{\alpha}_1}(\mathbf{x}) & \boldsymbol{\Phi}_2^{\boldsymbol{\alpha}_1}(\mathbf{x}) & \cdots & \boldsymbol{\Phi}_N^{\boldsymbol{\alpha}_1}(\mathbf{x}) \\ \boldsymbol{\Phi}_1^{\boldsymbol{\alpha}_2}(\mathbf{x}) & \boldsymbol{\Phi}_2^{\boldsymbol{\alpha}_2}(\mathbf{x}) & \cdots & \boldsymbol{\Phi}_N^{\boldsymbol{\alpha}_2}(\mathbf{x}) \\ \vdots & \vdots & \ddots & \vdots \\ \boldsymbol{\Phi}_1^{\boldsymbol{\alpha}_L}(\mathbf{x}) & \boldsymbol{\Phi}_2^{\boldsymbol{\alpha}_L}(\mathbf{x}) & \cdots & \boldsymbol{\Phi}_N^{\boldsymbol{\alpha}_L}(\mathbf{x}) \end{pmatrix} \begin{pmatrix} u_1 \\ u_2 \\ \vdots \\ u_N \end{pmatrix} \tag{2.10}$$

where $\boldsymbol{\alpha}_2 = (1,0)$, $\boldsymbol{\alpha}_3 = (0,1)$, …, $\boldsymbol{\alpha}_L = (0,m)$ when the mth order polynomial vector $\mathbf{p}_m$, $\boldsymbol{\alpha}_1 = (0,0)$ is applied for the 2D case. Here, the generalized nodal shape function $\boldsymbol{\Phi}_I^{\boldsymbol{\alpha}}(\mathbf{x})$ denotes the $\boldsymbol{\alpha}$th derivative of the shape function at node I defined as

$$\boldsymbol{\Phi}_I^{\boldsymbol{\alpha}}(\mathbf{x}) = \boldsymbol{\alpha}!\mathbf{e}_{\boldsymbol{\alpha}}^\top \mathbf{M}^{-1}(\mathbf{x})\mathbf{p}(\mathbf{x}_I;\mathbf{x}) w\left(\frac{\mathbf{x}_I - \mathbf{x}}{\rho_{\mathbf{x}}}\right) \tag{2.11}$$

where $\mathbf{e}_{\boldsymbol{\alpha}}^\top = [0, \dots, 1, \dots, 0]$ has only one nonzero term of 1 at the $\boldsymbol{\alpha}$th slot in lexicographic order. The first low of the generalized shape function matrix of Eq. (2.10) gives the zeroth-order shape function while the $\boldsymbol{\alpha}$th low yields the $\boldsymbol{\alpha}$th-order derivative shape function. Notice that the $\boldsymbol{\alpha}$th-order derivative shape function is an approximation of the derivative function of the zeroth-order shape function in a sense of the Taylor theorem; it has the consistency which guarantees the reproducing property for any function or its derivatives within the order of consistency of Taylor polynomial. This enables the strong-form collocation method to properly discretize the governing equations given in a differential form. In the conventional weak form based meshfree methods and other strong-form based meshfree methods [6,26], only the first low of the coefficient matrix of Eq. (2.10) is taken for discretization and the derivative function is calculated by directly differentiating these zeroth-order shape functions. Although direct differentiation may increase the mathematical preciseness of derivative approximation, it may demand excessive computational cost which turns out to cause more troublesome computation in dealing with the second-order derivative function. Therefore, the particle derivative approximation given in Eq. (2.10) is very attractive discretization tool for the strong-form based particle methods, which is equipped with sufficient mathematical preciseness as well as excellent computational efficiency [7,8].

3. Multi-body contact

3.1. Problem description

We consider frictional contact between two deformable bodies as shown in Fig. 1. The domain $\Omega^{(i)}$, $i = 1,2$, is bounded by $\Gamma^{(i)}$, i.e., $\bar{\Omega}^{(i)} = \Omega^{(i)} \cup \Gamma^{(i)}$. Assume that $\Gamma^{(i)}$ is partitioned into $\Gamma_u^{(i)}$, $\Gamma_t^{(i)}$, and $\Gamma_c^{(i)}$, which are Dirichlet and Neumann boundary conditions and contact constraints, respectively, i.e., $\Gamma^{(i)} = \Gamma_u^{(i)} \cup \Gamma_t^{(i)} \cup \Gamma_c^{(i)}$ with $\Gamma_u^{(i)} \cap \Gamma_t^{(i)} = \Gamma_u^{(i)} \cap \Gamma_c^{(i)} = \Gamma_c^{(i)} \cap \Gamma_t^{(i)} = \emptyset$. Displacements $\bar{u}^{(i)}$ will be prescribed on $\Gamma_u^{(i)}$,

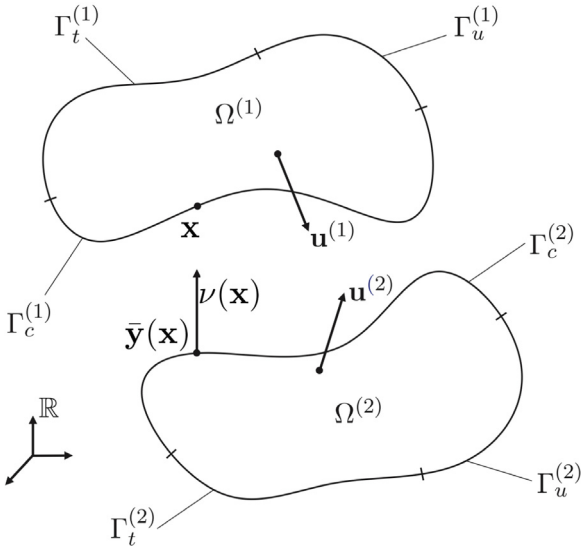

Fig. 1. Notation for two-body contact.

while tractions $\bar{t}^{(i)}$ are to be given on $\Gamma_t^{(i)}$. Finally, $\bar{\Omega} = \Omega^{(1)} \cup \Omega^{(2)}$ is used to denote the entire domain of interest.

The governing equations to find the displacement field $\mathbf{u}^{(i)}$ in $\Omega^{(i)}$ are given by

$$\operatorname{div}\boldsymbol{\sigma}^{(i)} + \mathbf{b}^{(i)} = 0 \quad \text{in } \Omega^{(i)} \tag{3.1}$$

where $\boldsymbol{\sigma}^{(i)}$ is the Cauchy stress tensor and $\mathbf{b}^{(i)}$ is a body force. For the constitutive assumption, we consider the linear elastic material, i.e.,

$$\boldsymbol{\sigma}^{(i)} = 2\mu\boldsymbol{\epsilon}^{(i)} + \lambda\operatorname{tr}(\boldsymbol{\epsilon}^{(i)})\mathbf{1} \tag{3.2}$$

where λ and μ are Lamé constants, $\mathbf{1}$ is the second-order identity tensor, and $\boldsymbol{\epsilon}^{(i)}$ is the strain tensor defined by $\boldsymbol{\epsilon}^{(i)} = (\nabla\mathbf{u}^{(i)} + (\nabla\mathbf{u}^{(i)})^\top)/2$. The Dirichlet and Neumann boundary conditions and contact constraints are given by

$$\begin{aligned} \mathbf{u}^{(i)} &= \bar{\mathbf{u}}^{(i)} \quad \text{on } \Gamma_u^{(i)}, \\ \boldsymbol{\sigma}^{(i)}\mathbf{n}^{(i)} &= \bar{\mathbf{t}}^{(i)} \quad \text{on } \Gamma_t^{(i)}, \\ \boldsymbol{\sigma}^{(i)}\mathbf{n}^{(i)} &= \mathbf{t}_c^{(i)} \quad \text{on } \Gamma_c^{(i)} \end{aligned} \tag{3.3}$$

where $\mathbf{n}$ is the unit outward normal vector to $\Omega^{(i)}$, $\bar{\mathbf{u}}^{(i)}$ is the prescribed displacement on $\Gamma_u^{(i)}$, $\bar{\mathbf{t}}^{(i)}$ is the prescribed traction on $\Gamma_t^{(i)}$, and $\mathbf{t}_c^{(i)}$ is the unknown contact traction on $\Gamma_c^{(i)}$.

3.2. Contact kinematics

To describe contact kinematics for two-body contact between two domains $\Omega^{(1)}$ and $\Omega^{(2)}$, we consider a point $\mathbf{x} \in \Gamma_c^{(1)}$ and assume for each such point $\mathbf{x}$, a corresponding point $\bar{\mathbf{y}}(\mathbf{x}) \in \Gamma_c^{(2)}$ which is closest to $\mathbf{x}$ in the Euclidean sense, i.e., $\bar{\mathbf{y}}(\mathbf{x}) = \arg\min\|\mathbf{x}-\mathbf{y}\|$. Notice that two surface normals $\mathbf{n}(\mathbf{x})$ and $\boldsymbol{\nu}(\mathbf{x})$ are associated with $\Gamma_c^{(1)}$ and $\Gamma_c^{(2)}$, respectively, i.e., $\boldsymbol{\nu}(\mathbf{x}) \approx -\mathbf{n}(\mathbf{x})$, as

$$\begin{aligned} \mathbf{n}^{(1)}(\mathbf{x}) &= \mathbf{n}(\mathbf{x}) \quad \text{on } \mathbf{x} \in \Gamma_c^{(1)}, \\ \mathbf{n}^{(2)}(\mathbf{x}) &= \boldsymbol{\nu}(\bar{\mathbf{y}}(\mathbf{x})) \quad \text{on } \mathbf{x} \in \Gamma_c^{(2)}, \\ \mathbf{n}^{(1)}(\mathbf{x}) &= -\mathbf{n}^{(2)}(\bar{\mathbf{y}}(\mathbf{x})) \end{aligned} \tag{3.4}$$

with the small displacement kinematic assumption, i.e., displacements are sufficiently small so that variations in contact points and normal can be neglected.

Given a displacement field $\mathbf{u}^{(i)} : \Gamma_c^{(i)} \to \mathbf{R}^2$, we define a gap function $g : \Gamma_c^{(i)} \to \mathbf{R}$ as follows. For all $\mathbf{x} \in \Gamma_c^{(1)}$,

$$g(\mathbf{x}) = g_0(\mathbf{x}) - [\mathbf{u}^{(1)}(\mathbf{x}) - \mathbf{u}^{(2)}(\bar{\mathbf{y}}(\mathbf{x}))] \cdot \boldsymbol{\nu}(\mathbf{x}), \tag{3.5}$$

where $g_0(\mathbf{x}) = (\mathbf{x} - \bar{\mathbf{y}}(\mathbf{x}))\boldsymbol{\nu}(\mathbf{x})$ denotes the initial gap between two bodies or gap at zero displacement. To define the normal contact conditions, the contact traction is decomposed into normal and tangential components via

$$\mathbf{t}_c^{(1)} = \mathbf{t}_N - \mathbf{t}_T = t_N \boldsymbol{\nu} - t_T \boldsymbol{\tau} \tag{3.6}$$

where $\boldsymbol{\nu}$ is the unit outward normal to Γ_c and $\boldsymbol{\tau}$ is the unit tangential vector defined as

$$\boldsymbol{\nu} = \mathbf{e}_3 \times \boldsymbol{\tau} \tag{3.7}$$

where $\mathbf{e}_3$ is the unit basis vector pointing out of the paper.

The gap function g and contact pressure t_N are then related through the Kuhn–Tucker complementary conditions:

$$g(\mathbf{x}) \le 0, \qquad t_N(\mathbf{x}) \ge 0, \qquad t_N g(\mathbf{x}) = 0. \tag{3.8}$$

Eq. $(3.8)_2$ refers to the fact that if there is contact then the pressure is compressive. Eq. $(3.8)_3$ is the requirement that the pressure is nonzero only when contact occurs (i.e., $g = 0$). Further, when $g < 0$, this condition requires that t_N be zero, consistent with an out-of-contact condition.

3.3. Penalty regularization

The contact constraints, i.e., both normal and frictional contact constraints, are regularized using the penalty method. A penalty regularization for the normal contact constraint is given by

$$t_N = \epsilon_N < g > \tag{3.9}$$

where $\epsilon_N > 0$ is the normal penalty parameter and $< \bullet >$ is the Macaulay bracket. The impenetrability condition is exactly satisfied as $\epsilon_N \to \infty$. The penalty regularization for the frictional contact constraint is given by

$$\begin{aligned} \boldsymbol{\Phi} &:= \|\mathbf{t}_T\| - \mu t_N \le 0, \\ \mathbf{v}_T - \dot{\zeta}\frac{\mathbf{t}_T}{\|\mathbf{t}_T\|} &= \frac{1}{\epsilon_T}\dot{\mathbf{t}}_T, \\ \dot{\zeta} &\ge 0, \\ \dot{\zeta}\boldsymbol{\Phi} &= 0 \end{aligned} \tag{3.10}$$

where $\epsilon_T > 0$ is the tangential penalty parameter, μ is the coefficient of friction, and ζ is a consistency parameter that expresses the collinearity of the slip displacement $\mathbf{u}_T$ and frictional stress $\mathbf{t}_T$ in rate form. Applying the backward Euler integrator to Eq. (3.10) yields

$$\begin{aligned} \boldsymbol{\Phi} &:= \|\mathbf{t}_T\| - \mu t_N \le 0, \\ \mathbf{t}_T &= \epsilon_T \left(\mathbf{u}_T - \Delta\zeta \frac{\mathbf{t}_T}{\|\mathbf{t}_T\|} \right), \\ \Delta\zeta &\ge 0, \\ \Delta\zeta\boldsymbol{\Phi} &= 0. \end{aligned} \tag{3.11}$$

A trial state/return mapping algorithm is employed to determine the Coulomb frictional traction. For implementation, the computational algorithm for Coulomb frictional traction is then given by:

1. The trial state is first computed by assuming no slip during the increment:
$$\begin{aligned} \mathbf{t}_T^{\text{trial}} &= \epsilon_T \mathbf{u}_T, \\ \boldsymbol{\Phi}^{\text{trial}} &= \|\mathbf{t}_T^{\text{trial}}\| - \mu t_N. \end{aligned} \tag{3.12}$$
where $\mathbf{u}_T = [\mathbf{1} - \boldsymbol{\nu} \otimes \boldsymbol{\nu}](\mathbf{u}^{(1)}(\mathbf{x}) - \mathbf{u}^{(2)}(\bar{\mathbf{y}}(\mathbf{x})))$ of point on $\mathbf{x} \in \Gamma_c^{(1)}$, relative to the opposing surface $\Gamma_c^{(2)}$. Note that the normal contact pressure t_N is previously given by $t_N = \epsilon_N < g >$ in Eq. (3.9).
2. Check the status of stick or slip condition based on the precomputed trial function $\boldsymbol{\Phi}^{\text{trial}}$:
$$\mathbf{t}_T = \begin{cases} \mathbf{t}_T^{\text{trial}} & \text{if } \boldsymbol{\Phi}^{\text{trial}} \le 0 \text{ (stick)}, \\ \mu t_N \dfrac{\mathbf{t}_T^{\text{trial}}}{\|\mathbf{t}_T^{\text{trial}}\|} & \text{otherwise (slip)}. \end{cases} \tag{3.13}$$

3.4. Discretization for two-body frictional contact

We present the discretization of the governing equations for the strong-form based meshfree collocation method. By substituting Eq. (3.2) into Eq. (3.1), the governing equations in Cartesian components can be written as

$$\mu u_{i,jj} + (\lambda + \mu) u_{j,ji} + b_i = 0 \quad \text{in } \Omega^{(i)} \tag{3.14}$$

where $i, j = 1, 2$ in two dimensions and the repeated subscript follows the summation convention. To solve the nonlinear systems of equations using a full Newton–Raphson iteration scheme, the residual $\mathbf{R}$ can be defined as

$$\mathbf{R}(\mathbf{u}) = \mathcal{L}(\mathbf{u}) - \mathcal{F}(\mathbf{u}) = \mathbf{0} \tag{3.15}$$

which is a nonlinear function of the solution vector $\mathbf{u}$ and $\mathcal{F}$ is nonlinear due to the presence of contact tractions. Applying the Newton–Raphson scheme to Eq. (3.15) in iteration j yields

$$\mathbf{R}(\mathbf{u}_j) + \left.\frac{\partial \mathbf{R}}{\partial \mathbf{u}}\right|_j \delta\mathbf{u} = \mathbf{0} \tag{3.16}$$

followed by the update

$$\mathbf{u}_{j+1} = \mathbf{u}_j + \delta\mathbf{u}, \tag{3.17}$$

in which $\frac{\partial \mathbf{R}}{\partial \mathbf{u}}$ is the tangent stiffness matrix $\mathbf{K}$, i.e., $\mathbf{K} = \frac{\partial \mathbf{R}}{\partial \mathbf{u}}$. For convenience, we define $Y = Y_i \cup Y_d \cup Y_t \cup Y_c$ where Y_i, Y_d, Y_t, and Y_c are sets of interior nodes, Dirichlet boundary nodes, Neumann boundary nodes, and nodes on contact surface Γ_c, respectively. The tangent stiffness matrix $\mathbf{K}$ is composed of the matrices $\mathbf{K}^{\text{int}}$, $\mathbf{K}^{\text{D}}$, $\mathbf{K}^{\text{N}}$, and $\mathbf{K}^{\text{c}}$ as shown in Eq. (4.20) in [25]. In the following, we provide the components of $\mathbf{K}$.

For simplicity, we denote $\boldsymbol{\Phi}^{\alpha}_{IJ} = \boldsymbol{\Phi}^{\alpha}_{J}(\mathbf{x}_I)$. Substituting Eq. (2.9) into Eq. (3.14) yields the discrete form of equations which are given by

$$\begin{aligned} &\sum_{J=1}^{N} \{[(\lambda + 2\mu)\boldsymbol{\Phi}^{(2,0)}_{IJ} + \mu\boldsymbol{\Phi}^{(0,2)}_{IJ}]u_{1I} + (\lambda + \mu)\boldsymbol{\Phi}^{(1,1)}_{IJ} u_{2I}\} + b_1(\mathbf{x}_I) = 0, \\ &\sum_{J=1}^{N} \{(\lambda + \mu)\boldsymbol{\Phi}^{(1,1)}_{IJ} u_{1I} + [\mu\boldsymbol{\Phi}^{(2,0)}_{IJ} + (\lambda + 2\mu)\boldsymbol{\Phi}^{(0,2)}_{IJ}]u_{2I}\} + b_2(\mathbf{x}_I) = 0 \end{aligned} \tag{3.18}$$

for the interior nodes $\mathbf{x}_J \in Y_i$. The components of the matrix $\mathbf{K}^{\text{int}}$ are

$$\begin{aligned} &K^{\text{int}}_{I1J1} = [(\lambda + 2\mu)\boldsymbol{\Phi}^{(2,0)}_{IJ} + \mu\boldsymbol{\Phi}^{(0,2)}_{IJ}], \quad K^{\text{int}}_{I2J1} = (\lambda + \mu)\boldsymbol{\Phi}^{(1,1)}_{IJ}, \\ &K^{\text{int}}_{I1J2} = (\lambda + \mu)\boldsymbol{\Phi}^{(1,1)}_{IJ}, \quad K^{\text{int}}_{I2J2} = \mu\boldsymbol{\Phi}^{(2,0)}_{IJ} + (\lambda + 2\mu)\boldsymbol{\Phi}^{(0,2)}_{IJ}. \end{aligned} \tag{3.19}$$

The discrete form of the Dirichlet boundary condition can be obtained by substituting Eq. (2.9) into Eq. $(3.3)_1$ as

$$\sum_{J=1}^{N} \boldsymbol{\Phi}^{(0,0)}_{IJ} u_{1I} - \bar{u}_{1I}(\mathbf{x}_J) = 0, \quad \sum_{J=1}^{N} \boldsymbol{\Phi}^{(0,0)}_{IJ} u_{2I} - \bar{u}_{2I}(\mathbf{x}_J) = 0 \tag{3.20}$$

for $\mathbf{x}_J \in Y_d$. The components of the matrix $\mathbf{K}^D$ are

$$K^D_{I1J1} = \boldsymbol{\Phi}^{(0,0)}_{IJ}, \qquad K^D_{I2J2} = \boldsymbol{\Phi}^{(0,0)}_{IJ}. \tag{3.21}$$

Similarly, for the discretization of the Neumann boundary condition, i.e., Eq. $(3.3)_2$, substituting Eq. (3.2) into Eq. $(3.3)_2$ yields

$$\mu(u_{i,j} + u_{j,i})n_j + \lambda\delta_{ij} n_j (u_{k,k}) = \bar{t}_i \quad \text{on } \Gamma_t^{(i)} \tag{3.22}$$

where δ_{ij} is the Kronecker delta. For the discretization of Eq. (3.22), substituting Eq. (2.9) into Eq. (3.22) results in

$$\begin{aligned} &\sum_{J=1}^{N} \{[(\lambda + 2\mu)\boldsymbol{\Phi}^{(1,0)}_{IJ} n_1 + \mu\boldsymbol{\Phi}^{(0,1)}_{IJ} n_2]u_{1I} \\ &\quad + [\lambda\boldsymbol{\Phi}^{(0,1)}_{IJ} n_1 + \mu\boldsymbol{\Phi}^{(1,0)}_{IJ} n_2]u_{2I}\} - t_1(\mathbf{x}_I) = 0, \\ &\sum_{J=1}^{N} \{[\mu\boldsymbol{\Phi}^{(0,1)}_{IJ} n_1 + \lambda\boldsymbol{\Phi}^{(1,0)}_{IJ} n_2]u_{1I} \\ &\quad + [(\lambda + 2\mu)\boldsymbol{\Phi}^{(0,1)}_{IJ} n_2 + \mu\boldsymbol{\Phi}^{(1,0)}_{IJ} n_1]u_{2I}\} - t_2(\mathbf{x}_I) = 0 \end{aligned} \tag{3.23}$$

for $\mathbf{x}_J \in Y_i$. The components of the matrix $\mathbf{K}^N$ are

$$K^N_{I1J1} = (\lambda+2\mu)\Phi^{(1,0)}_{IJ} n_1 + \mu\Phi^{(0,1)}_{IJ} n_2, \quad K^N_{I2J1} = \lambda\Phi^{(0,1)}_{IJ} n_1 + \mu\Phi^{(1,0)}_{IJ} n_2,$$
$$K^N_{I1J2} = \mu\Phi^{(0,1)}_{IJ} n_1 + \lambda\Phi^{(1,0)}_{IJ} n_2, \quad K^N_{I2J2} = (\lambda+2\mu)\Phi^{(0,1)}_{IJ} n_2 + \mu\Phi^{(1,0)}_{IJ} n_1. \tag{3.24}$$

To model normal and tangential constraints on the contact surface, we replace $\mathbf{t}_c$ with $\mathbf{t}_c = \mathbf{t}_N - \mathbf{t}_T$. Then, Eq. $(3.3)_3$ in Cartesian components can be written as

$$\mu(u_{i,j} + u_{j,i})n_j + \lambda\delta_{ij} n_j (u_{k,k}) - t_N \nu_i + t_T \tau_i = 0 \quad \text{on } \Gamma_c^{(i)}. \tag{3.25}$$

Applying Eq. (3.9) to t_N and Eq. (3.12) and (3.13) to t_T yields

$$\mu(u_{i,j} + u_{j,i})n_j + \lambda\delta_{ij} n_j (u_{k,k}) - \epsilon_N < g(\mathbf{x}_J) > n_i + t_T^{\text{trial}} \tau_i = 0. \tag{3.26}$$

For the stick case,

$$\mu(u_{i,j} + u_{j,i})n_j + \lambda\delta_{ij} n_j (u_{k,k}) - \epsilon_N < g(\mathbf{x}_J) > \nu_i + H(g(\mathbf{x}_J)) t_T^{\text{trial}} \tau_i = 0. \tag{3.27}$$

For the discretization of Eq. (3.27), substituting Eq. (2.9) into Eq. (3.27) results in

$$\sum_{J=1}^{N} \{[(\lambda+2\mu)\Phi^{(1,0)}_{IJ} n_1 + \mu\Phi^{(0,1)}_{IJ} n_2]\delta u_{1I} + [\lambda\Phi^{(0,1)}_{IJ} n_1 + \mu\Phi^{(1,0)}_{IJ} n_2]\delta u_{2I}\}$$
$$+ \epsilon_N H(g(\mathbf{x}_J))(\delta\mathbf{u}(\mathbf{x}_J)\cdot\boldsymbol{\nu})\nu_1 + \epsilon_T H(g(\mathbf{x}_J))(\delta\mathbf{u}\cdot\boldsymbol{\tau})\tau_1 = 0,$$
$$\sum_{J=1}^{N} \{[\mu\Phi^{(0,1)}_{IJ} n_1 + \lambda\Phi^{(1,0)}_{IJ} n_2]\delta u_{1I} + [(\lambda+2\mu)\Phi^{(0,1)}_{IJ} n_2 + \mu\Phi^{(1,0)}_{IJ} n_1]\delta u_{2I}\}$$
$$+ \epsilon_N H(g(\mathbf{x}_J))(\delta\mathbf{u}(\mathbf{x}_J)\cdot\boldsymbol{\nu})\nu_2 + \epsilon_T H(g(\mathbf{x}_J))(\delta\mathbf{u}\cdot\boldsymbol{\tau})\tau_2 = 0 \tag{3.28}$$

for $\mathbf{x}_J \in Y_c$ in the case of stick region. Here, $\delta\mathbf{u} = \delta\mathbf{u}^{(1)}(\mathbf{x}) - \delta\mathbf{u}^{(2)}(\bar{\mathbf{y}}(\mathbf{x}))$ which means that $\mathbf{x} \in \Gamma_c^{(1)}$ and $\bar{\mathbf{y}}(\mathbf{x}) \in \Gamma_c^{(2)}$. The components of the matrix $\mathbf{K}^c$ for the stick case are

$$K^c_{I1J1} = K^N_{I1J1} + K^{stick}_{I1J1}, \quad K^c_{I2J1} = K^N_{I2J1} + K^{stick}_{I2J1},$$
$$K^c_{I1J2} = K^N_{I1J2} + K^{stick}_{I1J2}, \quad K^c_{I2J2} = K^N_{I2J2} + K^{stick}_{I2J2}. \tag{3.29}$$

where K^N_{I1J1}, K^N_{I2J1}, K^N_{I1J2}, and K^N_{I2J2} can be obtained from Eq. (3.24). The components of the matrix $\mathbf{K}^{stick}$ in Eq. (3.29) are defined as

$$K^{stick}_{I1J1} = (\Phi^{(0,0)}_{IJ} - \Phi^{(0,0)}_{I'J})H(g(\mathbf{x}_J)) + [\epsilon_N \nu_1\nu_1 + \epsilon_T \tau_1\tau_1],$$
$$K^{stick}_{I2J1} = (\Phi^{(0,0)}_{IJ} - \Phi^{(0,0)}_{I'J})H(g(\mathbf{x}_J)) + [\epsilon_N \nu_2\nu_1 + \epsilon_T \tau_2\tau_1],$$
$$K^{stick}_{I1J2} = (\Phi^{(0,0)}_{IJ} - \Phi^{(0,0)}_{I'J})H(g(\mathbf{x}_J)) + [\epsilon_N \nu_1\nu_2 + \epsilon_T \tau_1\tau_2],$$
$$K^{stick}_{I2J2} = (\Phi^{(0,0)}_{IJ} - \Phi^{(0,0)}_{I'J})H(g(\mathbf{x}_J)) + [\epsilon_N \nu_2\nu_2 + \epsilon_T \tau_2\tau_2]. \tag{3.30}$$

where $\Phi^{(0,0)}_{IJ}$ is the interpolation operator for $\mathbf{x} \in \Gamma_c^{(1)}$, while $\Phi^{(0,0)}_{I'J}$ is the interpolation of corresponding contact node for $\bar{\mathbf{y}}(\mathbf{x}) \in \Gamma_c^{(2)}$. The components of $\mathbf{f}^c_{stick}$ vector are

$$t_1^c(\mathbf{x}_J) = \epsilon_N < g(\mathbf{x}_J) > \nu_1 - \epsilon_T H(g(\mathbf{x}_J))(u_k\tau_k)\tau_1,$$
$$t_2^c(\mathbf{x}_J) = \epsilon_N < g(\mathbf{x}_J) > \nu_2 - \epsilon_T H(g(\mathbf{x}_J))(u_k\tau_k)\tau_2.$$

for the slip case,

$$\mu(u_{i,j} + u_{j,i})n_j + \lambda\delta_{ij} n_j (u_{k,k}) - \epsilon_N < g(\mathbf{x}_J) > \nu_i + \mu t_N \text{sign}(t_T^{\text{trial}})\tau_i = 0. \tag{3.31}$$

For the discretization of Eq. (3.31), substituting Eq. (2.9) into Eq. (3.31) results in

$$\sum_{J=1}^{N} \{[(\lambda+2\mu)\Phi^{(1,0)}_{IJ} n_1 + \mu\Phi^{(0,1)}_{IJ} n_2]\delta u_{1I} + [\lambda\Phi^{(0,1)}_{IJ} n_1 + \mu\Phi^{(1,0)}_{IJ} n_2]\delta u_{2I}\}$$
$$+ \epsilon_N H(g(\mathbf{x}_J))(\delta\mathbf{u}(\mathbf{x}_J)\cdot\boldsymbol{\nu})\nu_1$$
$$- \mu\epsilon_N H(g(\mathbf{x}_J))(\delta\mathbf{u}(\mathbf{x}_J)\cdot\boldsymbol{\nu})\text{sign}(\mathbf{u}\cdot\boldsymbol{\tau})\tau_1 = 0,$$
$$\sum_{J=1}^{N} \{[\mu\Phi^{(0,1)}_{IJ} n_1 + \lambda\Phi^{(1,0)}_{IJ} n_2]\delta u_{1I} + [(\lambda+2\mu)\Phi^{(0,1)}_{IJ} n_2 + \mu\Phi^{(1,0)}_{IJ} n_1]\delta u_{2I}\}$$
$$+ H(g(\mathbf{x}_J))\epsilon_N(\delta\mathbf{u}(\mathbf{x}_J)\cdot\boldsymbol{\nu})\nu_2$$
$$- \mu\epsilon_N H(g(\mathbf{x}_J))(\delta\mathbf{u}(\mathbf{x}_J)\cdot\boldsymbol{\nu})\text{sign}(\mathbf{u}\cdot\boldsymbol{\tau})\tau_2 = 0 \tag{3.32}$$

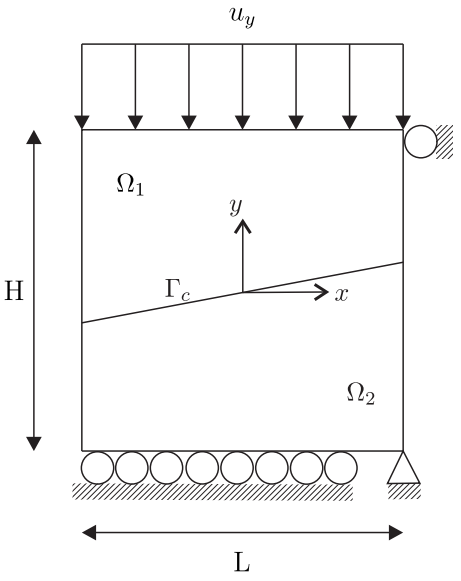

Fig. 2. Problem description of two-body frictional contact on an inclined surface.

for $\mathbf{x}_J \in Y_c$ in the case of slip region. The components of the matrix $\mathbf{K}^c$ for the slip case are

$$K^c_{I1J1} = K^N_{I1J1} + K^{slip}_{I1J1}, \quad K^c_{I2J1} = K^N_{I2J1} + K^{slip}_{I2J1},$$
$$K^c_{I1J2} = K^N_{I1J2} + K^{slip}_{I1J2}, \quad K^c_{I2J2} = K^N_{I2J2} + K^{slip}_{I2J2}. \tag{3.33}$$

The components of the matrix $\mathbf{K}^{slip}$ in Eq. (3.33) are defined as

$$K^{slip}_{I1J1} = (\Phi^{(0,0)}_{IJ} - \Phi^{(0,0)}_{I'J})H(g(\mathbf{x}_J)) + [\epsilon_N \nu_1\nu_1 - \mu\epsilon_N \text{sign}(u_k\tau_k)\nu_1\tau_1],$$
$$K^{slip}_{I2J1} = (\Phi^{(0,0)}_{IJ} - \Phi^{(0,0)}_{I'J})H(g(\mathbf{x}_J)) + [\epsilon_N \nu_2\nu_1 - \mu\epsilon_N \text{sign}(u_k\tau_k)\nu_2\tau_1],$$
$$K^{slip}_{I1J2} = (\Phi^{(0,0)}_{IJ} - \Phi^{(0,0)}_{I'J})H(g(\mathbf{x}_J)) + [\epsilon_N \nu_1\nu_2 - \mu\epsilon_N \text{sign}(u_k\tau_k)\nu_1\tau_2],$$
$$K^{slip}_{I2J2} = (\Phi^{(0,0)}_{IJ} - \Phi^{(0,0)}_{I'J})H(g(\mathbf{x}_J)) + [\epsilon_N \nu_2\nu_2 - \mu\epsilon_N \text{sign}(u_k\tau_k)\nu_2\tau_2]. \tag{3.34}$$

The components of the vector $\mathbf{f}^c_{slip}$ are

$$t_1^c(\mathbf{x}_J) = \epsilon_N < g(\mathbf{x}_J) > \nu_1 - \mu\epsilon_N < g(\mathbf{x}_J) > \text{sign}(u_k\tau_k)\tau_1,$$
$$t_2^c(\mathbf{x}_J) = \epsilon_N < g(\mathbf{x}_J) > \nu_2 - \mu\epsilon_N < g(\mathbf{x}_J) > \text{sign}(u_k\tau_k)\tau_2.$$

4. Numerical study

The proposed strong-form collocation algorithm is verified for two-body frictional contact and crack problems. Accuracy of the method is validated through the comparison with the results from Abaqus [27] using the plane stress element (CPS4R). Notice that a setting (i.e., material properties, frictional coefficient, boundary and loading conditions, etc.) in Abaqus is identical to that considered in the proposed collocation method.

4.1. Two-body frictional contact on an inclined surface

We examine the ability of the proposed collocation method to distinguish between stick and slip conditions for two-body contact problems. The method is applied to two-body frictional contact on an inclined surface used by Kim et al. [28] as a patch test for the verification of the mortar contact finite-element method (FEM).

A square domain of height H and width L is subjected to uniaxial compression as shown in Fig. 2. The interface is inclined as the contact surface Γ_c with the slope $m = 0.2$. The uniform compression $u_y = -0.01$ is applied at the top surface. The material properties are taken to be $E = 1.0$ and $\nu = 0.3$, and the height and width of the block are both

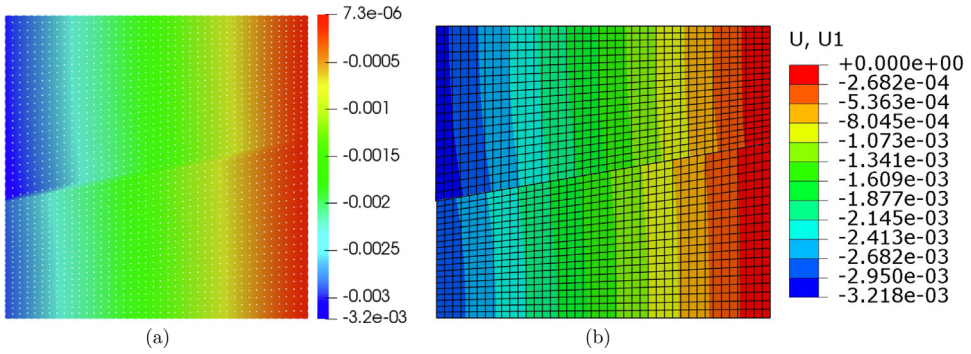

Fig. 3. The displacement u_x for $\mu = 0.19$: (a) collocation and (b) FEM.

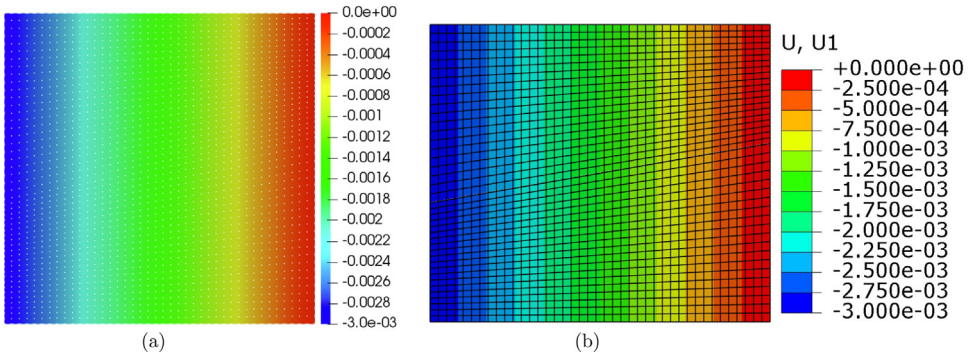

Fig. 4. The displacement u_x for $\mu = 0.21$: (a) collocation and (b) FEM.

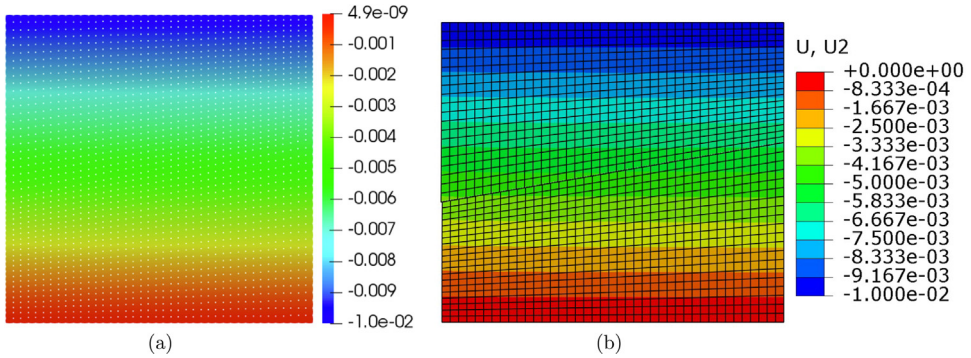

Fig. 5. The displacement u_y for $\mu = 0.19$: (a) collocation and (b) FEM.

taken to be $H/L = 1.0$. The normal and tangential penalty parameters are chosen to be $\epsilon_N = \epsilon_T = 10^6 E$. We use 2100 uniformly distributed collocation points for the test of this problem.

The displacement in the x-direction is displayed for $\mu = 0.19$ in Fig. 3 and for $\mu = 0.21$ in Fig. 4 along with the FEM solutions obtained from Abaqus. The results clearly show that the entire contact surface is under slip when $\mu = 0.19 < m = 0.2$ and under stick when $\mu = 0.21 > m = 0.2$, indicating that the meshfree collocation method can appropriately distinguish between stick and slip conditions. Our study reveals that the threshold friction coefficient for stick or slip is $\mu = m - (4.0 \times 10^{-14})$. Fig. 5 shows the displacements in the y-direction from both collocation and FEM for $\mu = 0.19$. Both results are almost consistent, indicating the accuracy of the proposed method. For further verification of the meshfree collocation method, the normal and tangential tractions on the contact surface are compared with FEM solutions for $\mu = 0.19$ in Fig. 6 and for $\mu = 0.21$ in Fig. 7. Both results are almost indistinguishable.

4.2. Frictional crack modeling

The performance of the proposed strong-form based contact formulation is verified for modeling frictional crack problems. We first begin by describing the modeling of a stationary crack with the strong-form based meshfree collocation method. This approach is incorporated into

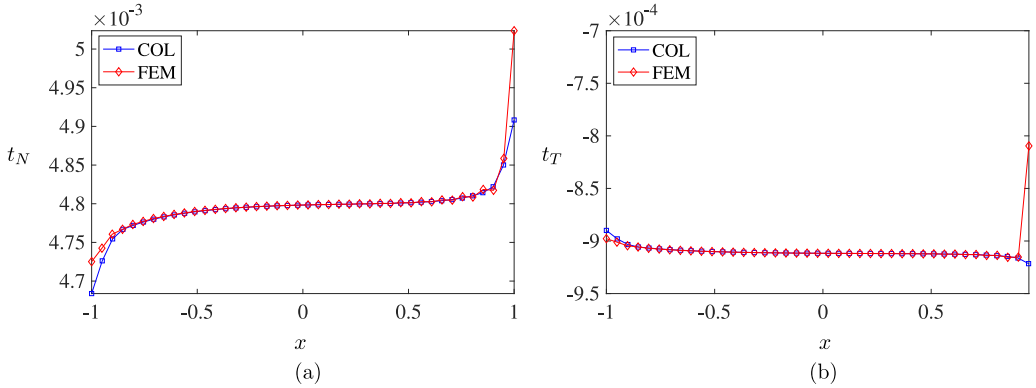

Fig. 6. Comparison of (a) normal traction t_N and (b) tangential traction t_T from the collocation (COL) method with FEM solutions from Abaqus for $\mu = 0.19$.

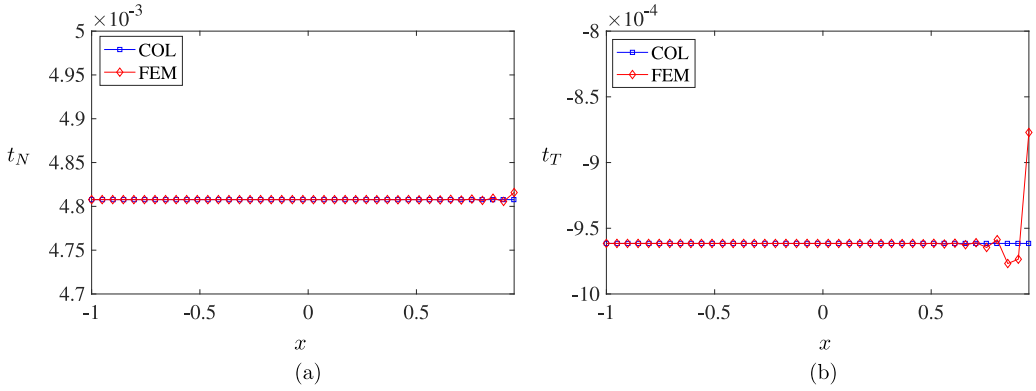

Fig. 7. Comparison of (a) normal traction t_N and (b) tangential traction t_T from the collocation (COL) method with FEM solutions from Abaqus for $\mu = 0.21$.

the modeling of the frictional crack, i.e., frictional contact on crack surfaces, in Section 4.2.3.

4.2.1. Crack modeling

We consider a domain Ω including a crack in the framework of the point collocation method based on the strong formulation. The governing equations in the domain Ω and Dirichlet and Neumann boundary conditions on the boundary Γ are given by Eq. (3.1) and Eqs. $(3.3)_1$ and $(3.3)_2$, respectively. We discretize the governing equation with the strong-form based collocation method for the interior, Dirichlet boundary, and Neumann boundary nodes based on the Eqs. (3.18), (3.20), and (3.23), respectively.

We consider a cracked body on a square domain as shown in Fig. 8. A crack surface $\Gamma_{cr}(= \Gamma_{cr^+} \cup \Gamma_{cr^-})$ is treated as a natural boundary condition. The traction-free condition is imposed on the crack surface Γ_{cr}, i.e.,

$$\begin{aligned} \boldsymbol{\sigma}\mathbf{n} = \bar{\mathbf{t}} = 0 \quad &\text{on } \Gamma_{cr}, \\ \boldsymbol{\sigma}\mathbf{n}^+ = \bar{\mathbf{t}}_{cr^+} = 0 \quad &\text{on } \Gamma_{cr^+}, \\ \boldsymbol{\sigma}\mathbf{n}^- = \bar{\mathbf{t}}_{cr^-} = 0 \quad &\text{on } \Gamma_{cr^-} \end{aligned} \tag{4.1}$$

where $\mathbf{n}^+$ and $\mathbf{n}^-$ are the outward surface normal vectors on Γ_{cr^+} and Γ_{cr^-}, respectively, and $\bar{\mathbf{t}}_{cr^+}$ and $\bar{\mathbf{t}}_{cr^-}$ are the tractions on Γ_{cr^+} and Γ_{cr^-}, respectively. The accuracy of the zero traction boundary conditions was examined in authors' previous studies [25]. It is obvious that the smooth solution fields near the zero traction boundary proved that the zero traction boundary conditions are captured accurately.

Imposing the traction-free condition in Eq. (4.1) on the crack surfaces generates the additional residual equations. However, it preserves the nodal displacements as one and only category of unknown variable to be determined from solving the global system of equations. The visibility criterion [3,4,29–31] is used to deal with the displacement discontinuity due to a crack. The idea of the criterion is to cut the domain of influence of the interested point and then ignore the nodes placed at the opposite side of the crack as shown in Fig. 8. The domain of influence of Ω_d is divided into Ω_d^+ and Ω_d^- by the crack line. The visibility criterion causes a discontinuity in the approximation around the crack tip. For this problem, analytical solutions for the displacement and stress fields [32] are given for mode I as

$$\begin{aligned} u_x &= \frac{K_I}{\mu}\sqrt{\frac{r}{2\pi}}\cos(\frac{\theta}{2})[1-2\nu+\sin^2(\frac{\theta}{2})], \\ u_y &= \frac{K_I}{\mu}\sqrt{\frac{r}{2\pi}}\sin(\frac{\theta}{2})[2-2\nu-\cos^2(\frac{\theta}{2})], \end{aligned} \tag{4.2}$$

$$\begin{aligned} \sigma_{xx} &= \frac{K_I}{\sqrt{2\pi r}}\cos(\frac{\theta}{2})[1-\sin(\frac{\theta}{2})\sin(\frac{3\theta}{2})], \\ \sigma_{yy} &= \frac{K_I}{\sqrt{2\pi r}}\cos(\frac{\theta}{2})[1+\sin(\frac{\theta}{2})\sin(\frac{3\theta}{2})], \\ \sigma_{xy} &= \frac{K_I}{\sqrt{2\pi r}}\cos(\frac{\theta}{2})\sin(\frac{\theta}{2})\cos(\frac{3\theta}{2}) \end{aligned} \tag{4.3}$$

and for mode II as

$$\begin{aligned} u_x &= \frac{K_{II}}{\mu}\sqrt{\frac{r}{2\pi}}\sin(\frac{\theta}{2})[2-2\nu+\cos^2(\frac{\theta}{2})], \\ u_y &= \frac{K_{II}}{\mu}\sqrt{\frac{r}{2\pi}}\cos(\frac{\theta}{2})[-1+2\nu+\sin^2(\frac{\theta}{2})], \end{aligned} \tag{4.4}$$

$$\begin{aligned} \sigma_{xx} &= \frac{-K_{II}}{\sqrt{2\pi r}}\sin(\frac{\theta}{2})[2+\cos(\frac{\theta}{2})\cos(\frac{3\theta}{2})], \\ \sigma_{yy} &= \frac{K_{II}}{\sqrt{2\pi r}}\sin(\frac{\theta}{2})\cos(\frac{\theta}{2})\cos(\frac{3\theta}{2}), \\ \sigma_{xy} &= \frac{K_{II}}{\sqrt{2\pi r}}\cos(\frac{\theta}{2})[1-\sin(\frac{\theta}{2})\sin(\frac{3\theta}{2})] \end{aligned} \tag{4.5}$$

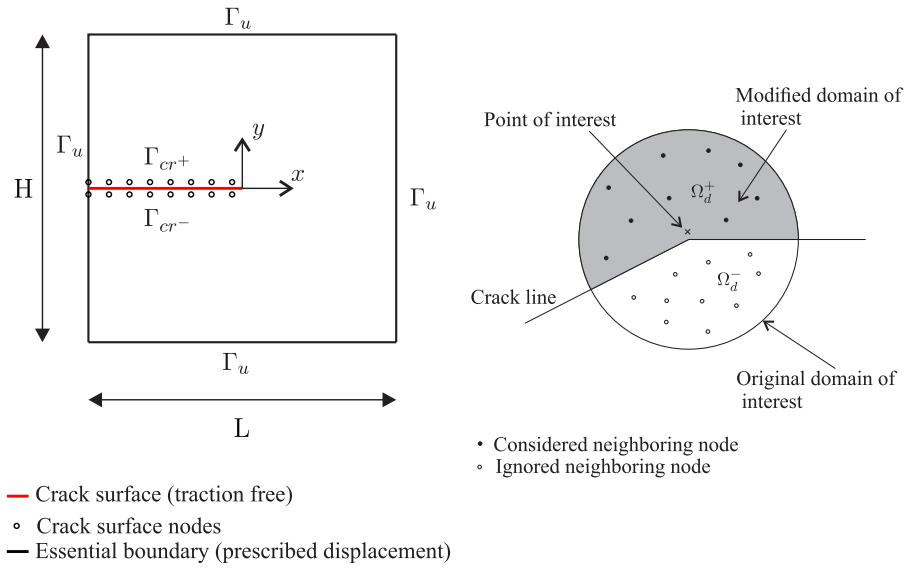

Fig. 8. Problem description of a near-tip field crack (left) and modification of the domain of influence near the crack tip via the visibility criterion (right). The crack is expressed by a straight-line segment (the solid red line) and crack surfaces are modeled by crack surface nodes on both sides of the line. The outward normal vector for each surface can then be uniquely defined, which is required to impose the traction-free condition. (For interpretation of the references to color in this figure legend, the reader is referred to the web version of this article.)

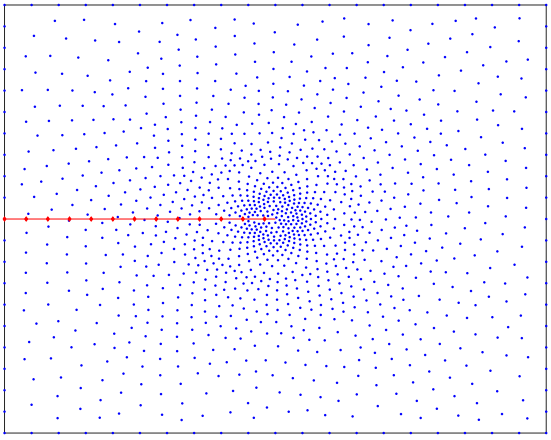

Fig. 9. Non-uniformly distributed 1293 collocation points refined near the crack tip. The coordinate of crack tip is (0, 0) which is located at the center of square patch.

where r is the distance from the crack-tip, θ is the angle measured from a line ahead of the crack, and μ is the shear modules. In addition, K_I and K_{II} are the stress intensity factors according to mode I and mode II loadings, respectively.

In this study, the domain form of the interaction integral is converted into a contour form of the interaction integral while it holds the same concept. To this end, equidistant collocation points are placed along the circular contour integration path to simplify the evaluation of integration weights in the contour integration. The analysis requires evaluations of the new conservation integral along a selected contour in the far field. In terms of mixed-mode [33] stress intensity factor solutions are obtained in terms of known auxiliary solutions and field variables along a selected contour. For a mixed-mode crack problem [33,34], we present the contour form of the interaction integral to determine K_I and K_{II}.

The relation between J-integral and stress intensity factors in mixed-mode crack problems is given by

$$J = \alpha(K_I^2 + K_{II}^2) \tag{4.6}$$

where $\alpha = (1-\nu)/E$ for plane strain and $\alpha = 1/E$ for plane stress. Upon considering the stress and displacement states consisting of the superposed state (1) and state (2) as

$$\boldsymbol{\sigma} = \boldsymbol{\sigma}^{(1)} + \boldsymbol{\sigma}^{(2)}, \qquad \mathbf{u} = \mathbf{u}^{(1)} + \mathbf{u}^{(2)},$$

J-integral for the stress can be computed by

$$\begin{aligned} J &= \alpha\left[(K_I^{(1)} + K_I^{(2)})^2 + (K_{II}^{(1)} + K_{II}^{(2)})^2\right] \\ &= \alpha\left[(K_I^{(1)})^2 + (K_{II}^{(1)})^2\right] + \alpha\left[(K_I^{(2)})^2 + (K_{II}^{(2)})^2\right] + 2\alpha(K_I^{(1)}K_I^{(2)} + K_{II}^{(1)}K_{II}^{(2)}) \\ &= J^{(1)} + J^{(2)} + I^{(1,2)} \end{aligned} \tag{4.7}$$

where $I^{(1,2)}$ is the interaction integral for state (1) and state (2) given by

$$I^{(1,2)} = 2\alpha(K_I^{(1)}K_I^{(2)} + K_{II}^{(1)}K_{II}^{(2)}). \tag{4.8}$$

To further express $I^{(1,2)}$ in terms of state (1) and state (2), by considering J-integral as

$$\begin{aligned} J &= \int\left(\frac{1}{2}\boldsymbol{\sigma} : \epsilon dy - \mathbf{t}\frac{\partial \mathbf{u}}{\partial x}d\Gamma\right) \\ &= \int\left[\frac{1}{2}(\boldsymbol{\sigma}^{(1)} + \boldsymbol{\sigma}^{(2)}) : (\boldsymbol{\epsilon}^{(1)} + \boldsymbol{\epsilon}^{(2)})dy - (\mathbf{t}^{(1)} + \mathbf{t}^{(2)})\frac{\partial(\mathbf{u}^{(1)} + \mathbf{u}^{(2)})}{\partial x}d\Gamma\right] \\ &= \int\left(\frac{1}{2}\boldsymbol{\sigma}^{(1)} : \boldsymbol{\epsilon}^{(1)}dy - \mathbf{t}^{(1)}\frac{\partial \mathbf{u}^{(1)}}{\partial x}d\Gamma\right) + \int\left(\frac{1}{2}\boldsymbol{\sigma}^{(2)} : \boldsymbol{\epsilon}^{(2)}dy - \mathbf{t}^{(2)}\frac{\partial \mathbf{u}^{(2)}}{\partial x}d\Gamma\right) \\ &+ \int\left[\frac{1}{2}\left(\boldsymbol{\sigma}^{(1)} : \boldsymbol{\epsilon}^{(2)} + \boldsymbol{\sigma}^{(2)} : \boldsymbol{\epsilon}^{(1)}\right)dy - \left(\mathbf{t}^{(1)}\frac{\partial \mathbf{u}^{(2)}}{\partial x} + \mathbf{t}^{(2)}\frac{\partial \mathbf{u}^{(1)}}{\partial x}\right)d\Gamma\right] \\ &= J^{(1)} + J^{(2)} + I^{(1,2)}, \end{aligned} \tag{4.9}$$

the interaction integral (4.8) can be rewritten as

$$\begin{aligned} I^{(1,2)} &= \int\left[\frac{1}{2}\left(\boldsymbol{\sigma}^{(1)} : \boldsymbol{\epsilon}^{(2)} + \boldsymbol{\sigma}^{(2)} : \boldsymbol{\epsilon}^{(1)}\right)dy - \left(\mathbf{t}^{(1)}\frac{\partial \mathbf{u}^{(2)}}{\partial x} + \mathbf{t}^{(2)}\frac{\partial \mathbf{u}^{(1)}}{\partial x}\right)d\Gamma\right] \\ &= \int\left[\left(\boldsymbol{\sigma}^{(2)} : \boldsymbol{\epsilon}^{(1)}\right)n_x - \left(\boldsymbol{\sigma}^{(1)}\mathbf{n}\frac{\partial \mathbf{u}^{(2)}}{\partial x} + \boldsymbol{\sigma}^{(2)}\mathbf{n}\frac{\partial \mathbf{u}^{(1)}}{\partial x}\right)\right]d\Gamma \\ &= \int\left(\sigma_{kk}^{(2)}\epsilon_{kk}^{(1)}\delta_{ij} - \sigma_{ij}^{(1)}\frac{\partial u_i^{(2)}}{\partial x_1} - \sigma_{ij}^{(2)}\frac{\partial u_i^{(1)}}{\partial x_1}\right)n_j d\Gamma \end{aligned} \tag{4.10}$$

where $dy = n_x d\Gamma$.

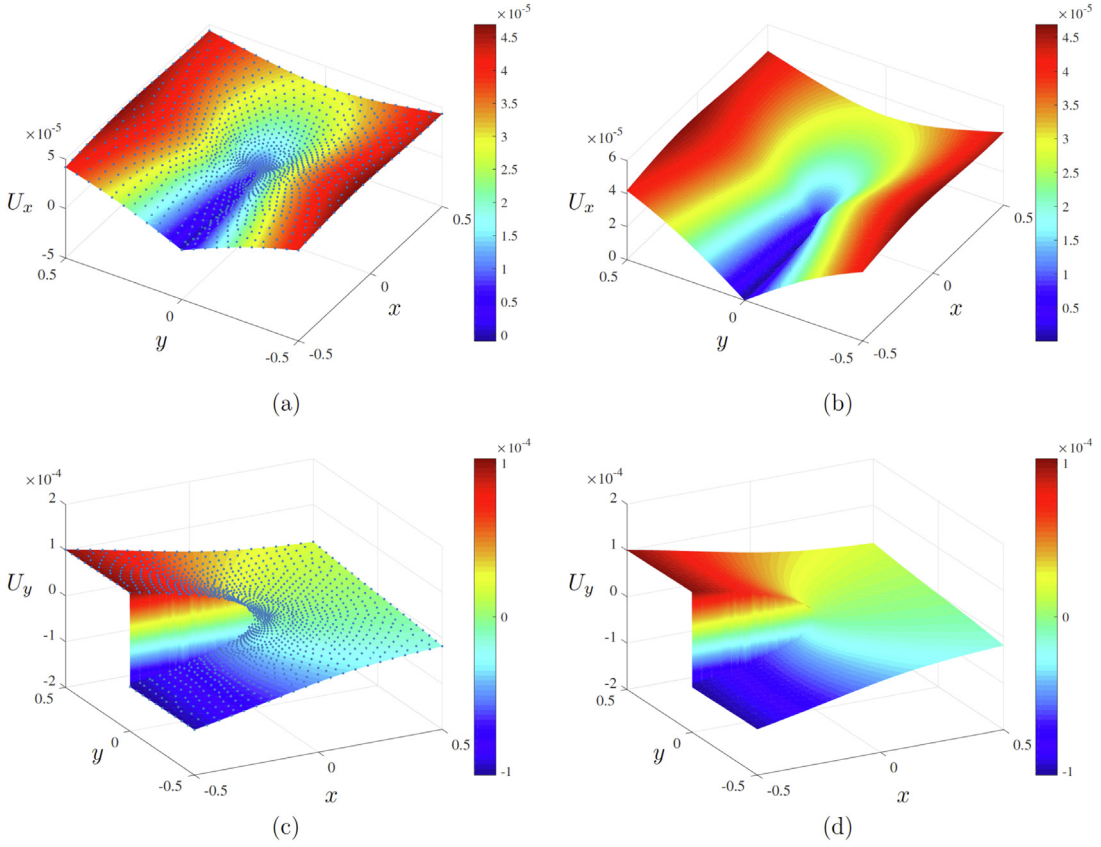

Fig. 10. Surface plots of the displacement fields for a square patch with near-tip field for mode *I*: (a) u_x (COL), (b) u_x (analytical), (c) u_y (COL), and (d) u_y (analytical).

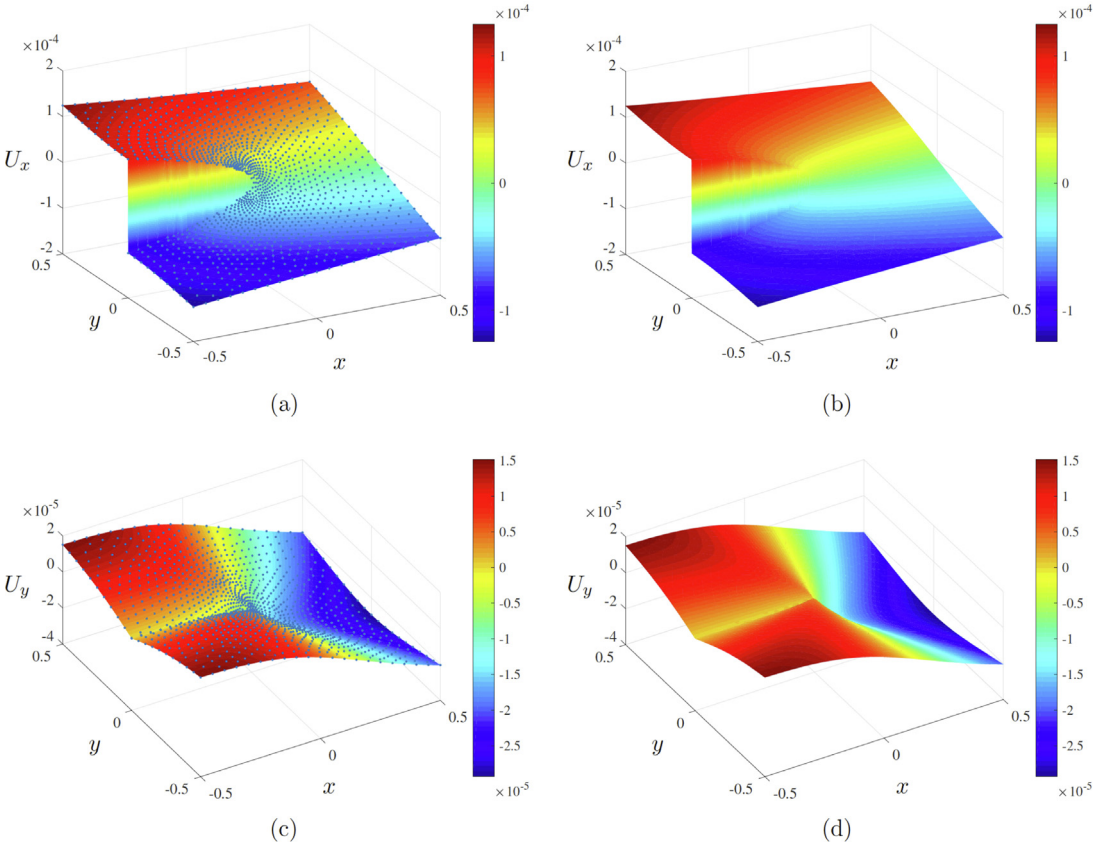

Fig. 11. Surface plots of the displacement fields for a square patch with near-tip field for mode *II*: (a) u_x (COL), (b) u_x (analytical), (c) u_y (COL), and (d) u_y (analytical).

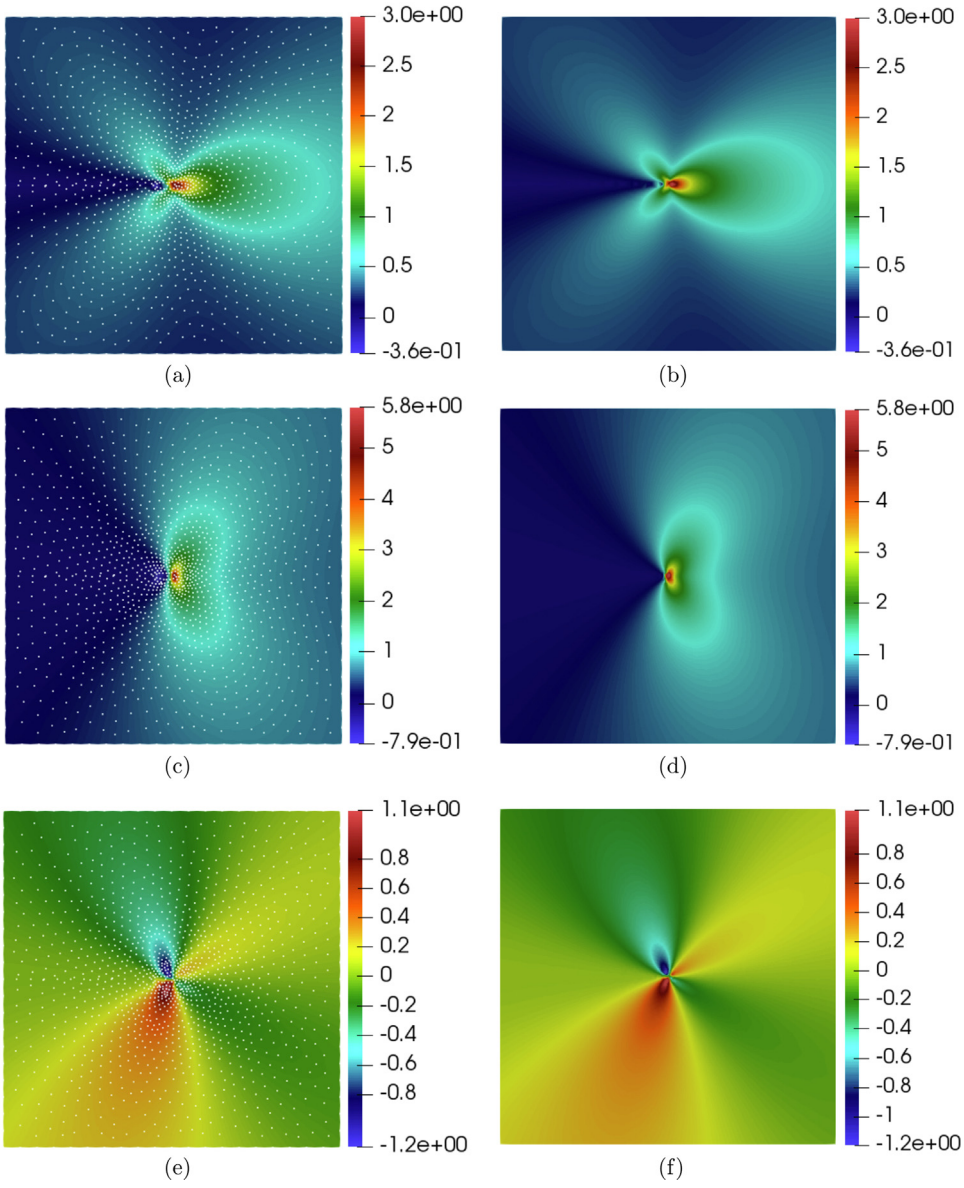

Fig. 12. Stress fields of a square patch with near-tip field for mode I: (a) σ_{xx} (COL), (b) σ_{xx} (analytical), (c) σ_{yy} (COL), (d) σ_{yy} (analytical), (e) σ_{xy} (COL), and (f) σ_{xy} (analytical).

Using Eqs. (4.8) and (4.10), we compute K_I and K_{II}. If $\mathbf{u}^{(2)}$ and $\boldsymbol{\sigma}^{(2)}$ are computed from pure mode I, $K_I^{(2)} = 1$ and $K_{II}^{(2)} = 0$. From Eq. (4.8), we have

$$K_I^{(1)} = \frac{I^{(1,2)}}{2\alpha}. \tag{4.11}$$

Similarly, if $\mathbf{u}^{(2)}$ and $\boldsymbol{\sigma}^{(2)}$ are computed from pure mode II, $K_I^{(2)} = 0$ and $K_{II}^{(2)} = 1$. From Eq. (4.8), we have

$$K_{II}^{(1)} = \frac{I^{(1,2)}}{2\alpha}. \tag{4.12}$$

Eventually, the interaction integral can be computed as

$$\begin{aligned} I^{(1,2)} = &\int \left(\sigma_{11}^{(2)}\epsilon_{11}^{(1)} + 2\sigma_{12}^{(2)}\epsilon_{12}^{(1)} + \sigma_{22}^{(2)}\epsilon_{22}^{(1)}\right) n_1 \\ &- \left[\left(\sigma_{11}^{(1)}n_1 + \sigma_{12}^{(1)}n_2\right)\frac{\partial u_1^{(2)}}{\partial x_1} + \left(\sigma_{21}^{(1)}n_1 + \sigma_{22}^{(1)}n_2\right)\frac{\partial u_2^{(2)}}{\partial x_1}\right] \\ &- \left[\left(\sigma_{11}^{(2)}n_1 + \sigma_{12}^{(2)}n_2\right)\frac{\partial u_1^{(1)}}{\partial x_1} + \left(\sigma_{21}^{(2)}n_1 + \sigma_{22}^{(2)}n_2\right)\frac{\partial u_2^{(1)}}{\partial x_1}\right] d\Gamma \\ \simeq &\sum^{N} \hat{I}^{(1,2)} d\Gamma. \end{aligned} \tag{4.13}$$

4.2.2. A square patch with near-tip field

To verify the performance of the strong-form meshfree collocation formulation for crack problems, we consider the problem of a square patch with boundary conditions from the closed form solutions for mode I and mode II which was used in [31,35].

As illustrated in Fig. 8, the square patch has height H and width L including a crack of length $L/2$. The crack tip is located at the center of the patch $(0,0)$. The material properties are taken to be $E = 10^4$ and $\nu = 0.3$, and the height and width of the block are taken to be $H/L = 1.0$. Along the boundaries of the patch, the known near-tip displacement fields, i.e., Eq. (4.2) for mode I and Eq. (4.4) for mode II, are prescribed as shown in Fig. 8. The stress intensity factor for mixed mode fracture is recalculated by the interaction integral (Eqs. (4.11)

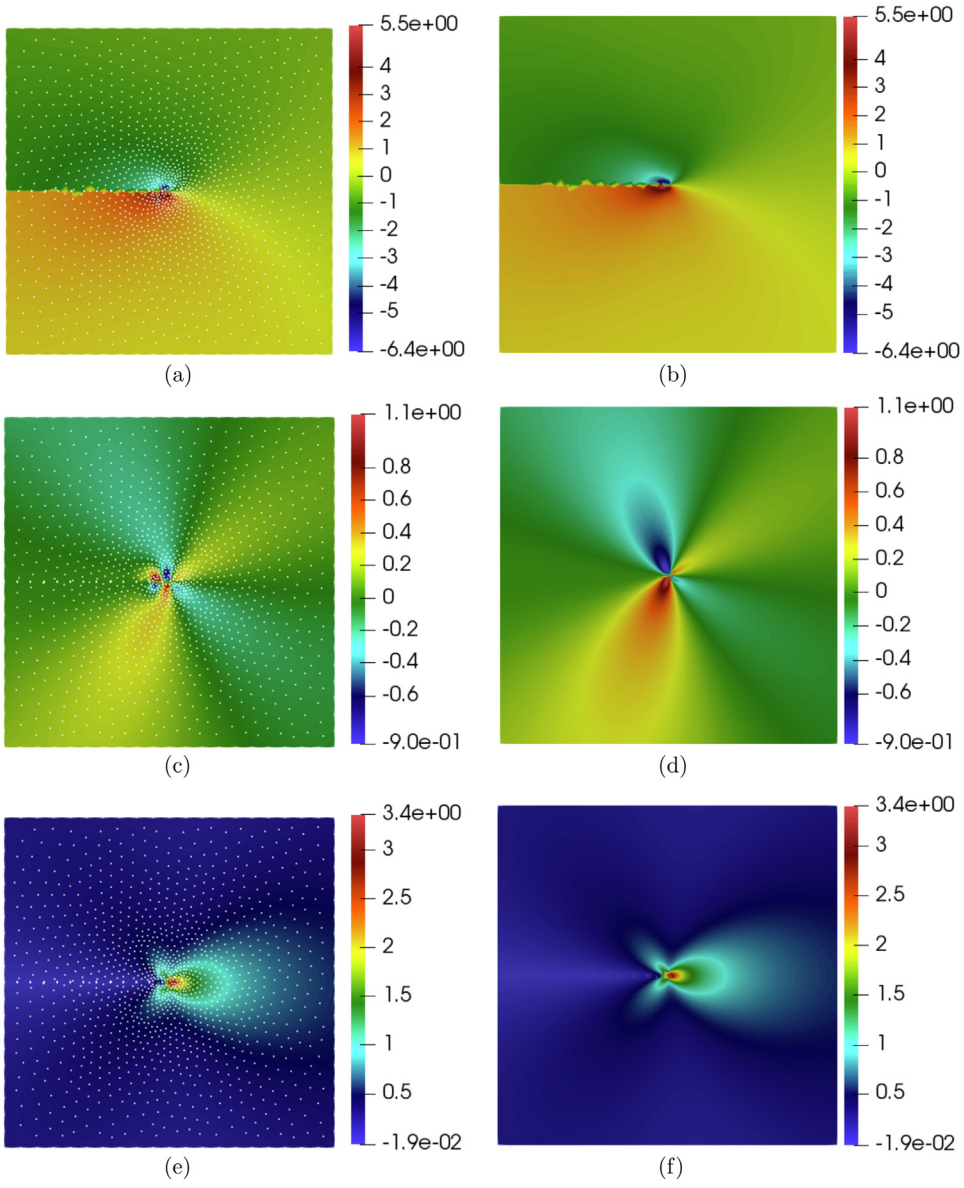

Fig. 13. Stress fields of a square patch with near-tip field for mode II: (a) σ_{xx} (COL), (b) σ_{xx} (analytical), (c) σ_{yy} (COL), (d) σ_{yy} (analytical), (e) σ_{xy} (COL), and (f) σ_{xy} (analytical).

and (4.12)) which is developed from the domain form of the interaction integral [36]. Table 1 presents the calculated stress intensity factors and L^2-norm errors of the displacement fields for mode I and mode II using the prescribed values of $K_I = 1.0$ and $K_{II} = 0.0$ for mode I and $K_I = 0.0$ and $K_{II} = 1.0$ for mode II. The calculated stress intensity factors agree well with the prescribed ones, i.e., the absolute error of K_I is less than 1%.

In Fig. 9, we display a model of non-uniformly distributed 1293 collocation points adaptively refined in the vicinity of the crack tip. The contour plots of the displacement fields by the proposed collocation method and their corresponding analytical solutions are shown in Figs. 10 and 11 for mode I and II, respectively. The displacement fields from the proposed method are almost indistinguishable with their analytical solutions. The contour plots of the stress fields are shown in Figs. 12 and 13 for mode I and II, respectively. All the results in these figures are qualitatively indistinguishable with their analytical solutions. Here, we calculated analytical solution for non-uniform distribution (see Fig. 9) and compared it with the proposed method. Fig. 14 shows that the crack-tip opening displacement u_y

Table 1
Stress intensity factors for mode I and II for a square patch with near-tip field.

Mode type	K_I	K_{II}	$\lvert e_{K_I} \rvert$	$\lvert e_{K_{II}} \rvert$	$\lVert e_{\mathbf{u}} \rVert_2$
Mode I	1.0095	0.0079	0.0095	0.0079	0.0066
Mode II	0.0044	1.013	0.0044	0.013	0.045

of the proposed collocation method agrees well with the closed-form solution. These results indicate that the proposed strong-form meshfree collocation method can model a crack with high accuracy. The relative errors in stress intensity factors for a mode I crack were studied for various polynomial bases and three uniform discretizations in Table 1 of Lee and Yoon [31]. For all the polynomial bases considered, the relative errors were less than 1% indicating acceptable accuracy of the proposed collocation method.

4.2.3. Frictional contact on a crack surface

In this section, the performance of the strong-form based contact formulation is verified for frictional contact on a crack surface. To do

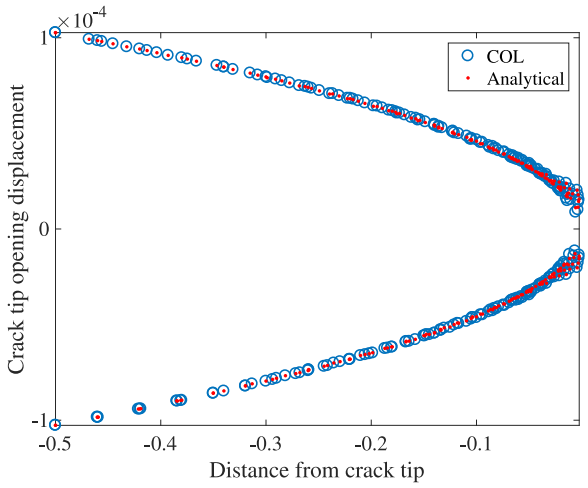

Fig. 14. The crack-tip opening displacement u_y for a square patch with near-tip field.

so, contact constrains in Eq. $(3.3)_3$ are imposed as a traction boundary condition on the crack surfaces. As a benchmark test, we examine frictional sliding across an internal crack surface as shown in Fig. 15. This problem was initially investigated by Dolbow et al. [36] and then used by other researchers including Liu and Borja [37], Annavarapu et al. [38], and Fei and Choo [39]. Here, we consider the problem of a square domain of height H and width L with a crack extending from the coordinates $(0.3, 0.3)$ and $(0.7, 0.7)$. The material properties are taken to be $E = 10^4$ and $\nu = 0.3$, and the height and width of the block are both taken to be $H/L = 1.0$. The normal and tangential penalty parameters are chosen to be $\epsilon_N = \epsilon_T = 10^7$, and the friction coefficient of the crack as $\mu = 0.1$. The uniform vertical displacement $u_y = -0.1$ is applied at the top surface as shown in the figure. The bottom surface is fixed.

In Fig. 16, we display non-uniformly distributed 1488 collocation points with refinement near crack tips used for this study. The comparison of horizontal and vertical displacement contours obtained using the collocation method and FEM using Abaqus are plotted in Figs. 17 and 18, respectively. The contour plots are in excellent agreement with those obtained by FEM, and confirm that the proposed method gives consistent solutions for the fictional crack problem. In the authors' previous work, the behaviors of the L_2 and L_∞ norm errors in the displacement and contact normal traction for uniformly [25] and randomly [40] distributed collocation points were investigated for Hertzian contact problem. The optimal convergence rates were observed with increasing the number of collocation points.

For further verification of the collocation method, the displacement fields of the proposed collocation method are compared with those of FEM at two different cross sections of the computational domain, subsequently referred to as Sections 1 and 2 in Fig. 15. Fig. 19(a) shows the comparison of the displacement fields along a horizontal line passing through crack surface, i.e., Section 1. Similarly, Fig. 19(b) compares the displacement fields for the collocation method and FEM along a vertical line passing through crack surface, i.e., Section 2. Despite minor discrepancies, both results agree well and are practically close. Moreover, the computational efficiency of the method was tested by measuring CPU wall-clock time for uniformly [25] and non-uniformly [40] distributed collocation points. The measured CPU wall-clock times for collocation points considered were comparable with the conventional finite element methods.

5. Conclusion

In this study, we introduced a two-body contact formulation for a strong-form meshfree collocation method to model frictional contact

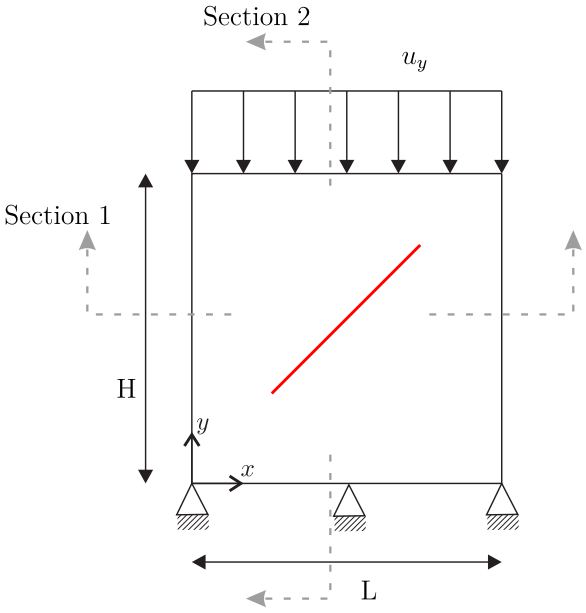

Fig. 15. Problem description of frictional crack.

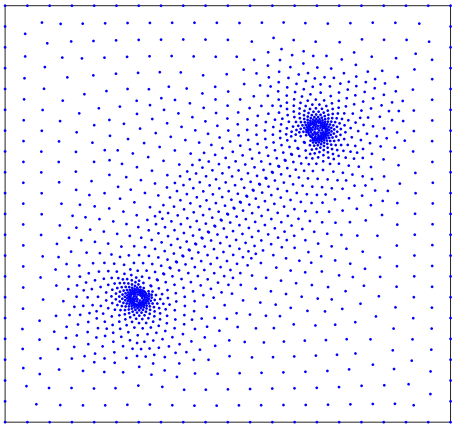

Fig. 16. Non-uniformly distributed 1488 collocation points for the inclined crack problem.

and frictional crack problems. It achieves truly meshfree features by only using nodes for discretization of the strong form. A line segment used for the recognition of the contact surface or crack is not associated with the node structure. Nonlinear contact constraints were directly imposed to the strong form as part of the traction boundary conditions. The strong form of the governing equation was then discretized with the strong-form based meshfree collocation method recently introduced. The performance of the strong-form based contact formulation was verified for frictional contact and crack problems via several numerical examples.

For two-body frictional contact, our simulation results showed that the method could capture well the stick–slip response on a block with an inclined contact surface. Unlike the previous study about frictional contact with a rigid obstacle [25], the frictional contact between two deformable bodies was considered. The displacement and traction were accurately computed even near boundary region; the tangential type jump in the x-directional displacement was successfully calculated and very stable traction responses were obtained in the vicinity of traction boundary without any surge in their values. In particular, the normal

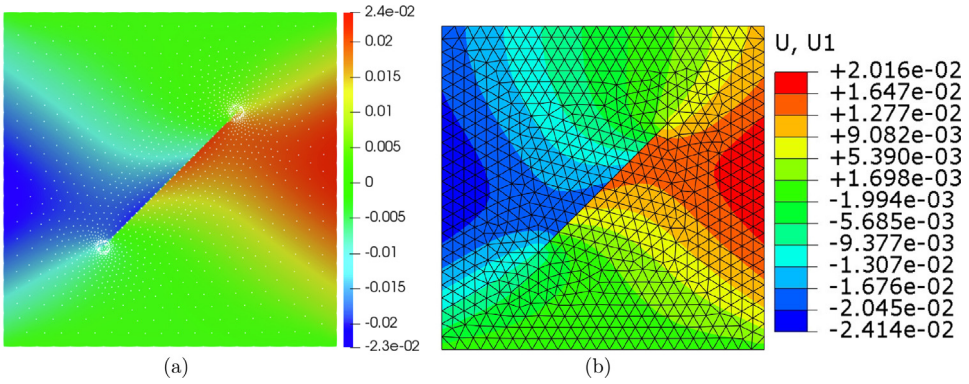

Fig. 17. Displacement u_x for frictional crack: (a) collocation method and (b) FEM.

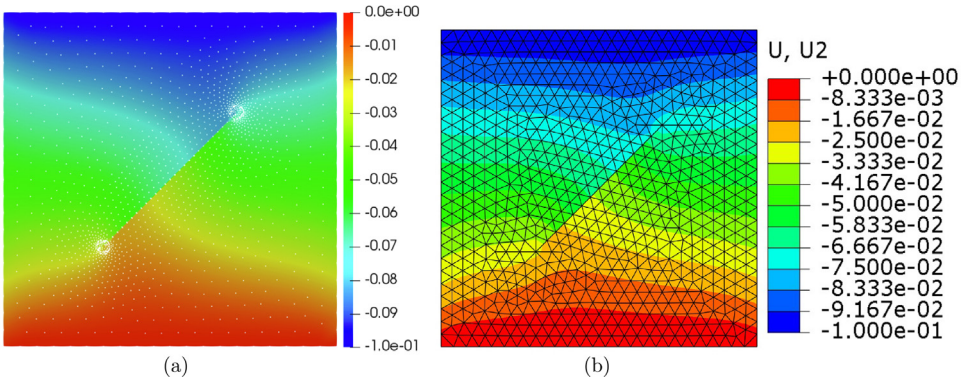

Fig. 18. Displacement u_y for frictional crack: (a) collocation method and (b) FEM.

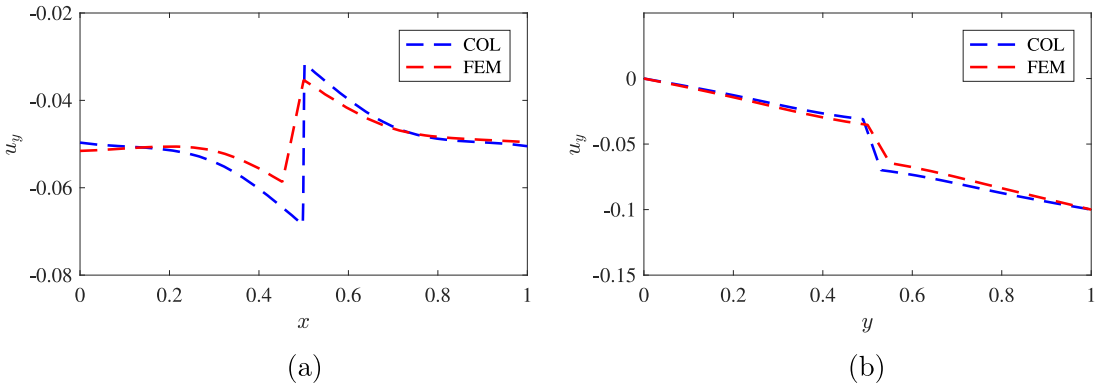

Fig. 19. Comparison of the collocation (COL) with FEM for frictional crack: (a) u_y along Section 1 and (b) u_y along Section 2.

and tangential tractions computed from the collocation method showed better profiles along the contact surface than those obtained from the FEM.

For a frictional crack, the penalty method for frictional contact and the visibility criterion for strong discontinuity modeling were successfully combined into the strong-form meshfree collocation method. The method examined frictional sliding across an internal crack surface. The computed y-directional displacements along the horizontal and vertical cross sections agree well with those from the FEM analysis and they sharply capture jump across the contact surface even with smaller smearing than the FEM. Also, the stress intensity factor was accurately reproduced with respect to the prescribed mode I and II near-tip fields.

These results show that the proposed strong-form based meshfree collocation method can be applied to model two-body frictional contact and crack problems. Future work will be focus on further verification of our algorithm to various contact problems and non-stationary cracks for elastic and inelastic materials in two or three dimensions. Such extension and application of the proposed algorithm to three-dimensions will not be significant challenges based on authors' previous work [12,41,42]. Moreover, we will develop a robust mathematical adaptive algorithm that can automatically refine collocation points in frictional contact or crack regions.

CRediT authorship contribution statement

Ashkan Almasi: Software, Visualization, Validation, Writing – original draft. **Young-Cheol Yoon:** Writing – original draft, Writing – review & editing. **Tae-Yeon Kim:** Writing – review & editing. **Tod A.**

Laursen: Writing – review & editing. **Jeong-Hoon Song:** Conceptualization, Methodology, Supervision, Writing – review & editing.

Declaration of competing interest

The authors declare that they have no known competing financial interests or personal relationships that could have appeared to influence the work reported in this paper.

Data availability

No data was used for the research described in the article.

References

[1] Ted Belytschko, Yun Yun Lu, Lei Gu, Element-free Galerkin methods, Internat. J. Numer. Methods Engrg. 37 (2) (1994) 229–256.

[2] Wing Kam Liu, Sukky Jun, Yi Fei Zhang, Reproducing kernel particle methods, Internat. J. Numer. Methods Fluids 20 (8–9) (1995) 1081–1106.

[3] M. Fleming, Y.A. Chu, B. Moran, T. Belytschko, Enriched element-free Galerkin methods for crack tip fields, Internat. J. Numer. Methods Engrg. 40 (8) (1997) 1483–1504.

[4] T. Belytschko, M. Fleming, Smoothing, enrichment and contact in the element-free Galerkin method, Comput. Struct. 71 (2) (1999) 173–195.

[5] E. Onate, S. Idelsohn, O.C. Zienkiewicz, R.L. Taylor, A finite point method in computational mechanics, applications to convective transport and fluid flow, Int. J. Numer. Methods Eng. 39 (22) (1996) 3839–3866.

[6] N.R. Aluru, A point collocation method based on reproducing kernel approximations, Internat. J. Numer. Methods Engrg. 47 (6) (2000) 1083–1121.

[7] Young-Cheol Yoon, Jeong-Hoon Song, Extended particle difference method for weak and strong discontinuity problems: Part I. Derivation of the extended particle derivative approximation for the representation of weak and strong discontinuities, Comput. Mech. 53 (6) (2014) 1087–1103a.

[8] Young-Cheol Yoon, Jeong-Hoon Song, Extended particle difference method for weak and strong discontinuity problems: Part II. Formulations and applications for various interfacial singularity problems, Comput. Mech. 53 (6) (2014) 1105–1128b.

[9] Young-Cheol Yoon, Jeong-Hoon Song, Extended particle difference method for moving boundary problems, Comput. Mech. 54 (3) (2014) 723–743.

[10] Young-Cheol Yoon, Sang-Ho Lee, Ted Belytschko, Enriched meshfree collocation method with diffuse derivatives for elastic fracture, Comput. Math. Appl. 51 (8) (2006) 1349–1366.

[11] Young-Cheol Yoon, Jeong-Hoon Song, Interface immersed particle difference method for weak discontinuity in elliptic boundary value problems, Comput. Methods Appl. Mech. Engrg. 375 (2021) 113650.

[12] Jeong-Hoon Song, Yao Fu, Tae-Yeon Kim, Yeong-Cheol Yoon, John G. Michopoulos, Timon Rabczuk, Phase field simulations of coupled microstructure solidification problems via the strong form particle difference method, Int. J. Mech. Mater. Des. 14 (4) (2018) 491–509.

[13] Peter Schaefferkoetter, John G. Michopoulos, Jeong-Hoon Song, Strong-form meshfree collocation method for non-equilibrium solidification of multi-component alloy, Eng. Comput. (2021) http://dx.doi.org/10.1007/s00366-021-01503-7.

[14] Andrew Beel, Jeong-Hoon Song, Strong-form meshfree collocation method for multibody thermomechanical contact, Eng. Comput. (2021) http://dx.doi.org/10.1007/s00366-021-01513-5.

[15] Sang-Ho Lee, Kyeong-Hwan Kim, Young-Cheol Yoon, Particle difference method for dynamic crack propagation, Int. J. Impact Eng. 87 (2016) 132–145.

[16] Young-Cheol Yoon, Kyeong-Hwan Kim, Sang-Ho Lee, Dynamic particle difference method for the analysis of proportionally damped system and cracked concrete beam, Int. J. Fract. 203 (1) (2017) 237–262.

[17] Kyeong-Hwan Kim, Young-Cheol Yoon, Sang-Ho Lee, Analysis of concrete tensile failure using dynamic particle difference method under high loading rates, Int. J. Impact Eng. 150 (2021) 103802.

[18] Timon Rabczuk, Goangseup Zi, Stephane Bordas, Hung Nguyen-Xuan, A simple and robust three-dimensional cracking-particle method without enrichment, Comput. Methods Appl. Mech. Engrg. 199 (37–40) (2010) 2437–2455.

[19] Timon Rabczuk, Ted Belytschko, Cracking particles: A simplified meshfree method for arbitrary evolving cracks, Internat. J. Numer. Methods Engrg. 61 (13) (2004) 2316–2343.

[20] Pedro Areias, Timon Rabczuk, F.J.M. Queirós de Melo, J. César De Sá, Coulomb frictional contact by explicit projection in the cone for finite displacement quasi-static problems, Comput. Mech. 55 (1) (2015) 57–72.

[21] N. Nguyen-Thanh, K. Zhou, X. Zhuang, P. Areias, H. Nguyen-Xuan, Y. Bazilevs, Timon. Rabczuk, Isogeometric analysis of large-deformation thin shells using RHT-splines for multiple-patch coupling, Comput. Methods Appl. Mech. Engrg. 316 (2017) 1157–1178.

[22] L. De Lorenzis, J.A. Evans, Thomas J.R. Hughes, A. Reali, Isogeometric collocation: Neumann boundary conditions and contact, Comput. Methods Appl. Mech. Engrg. 284 (2015) 21–54.

[23] R. Kruse, N. Nguyen-Thanh, L. De Lorenzis, Thomas J.R. Hughes, Isogeometric collocation for large deformation elasticity and frictional contact problems, Comput. Methods Appl. Mech. Engrg. 296 (2015) 73–112.

[24] Oliver Weeger, Sai-Kit Yeung, Martin L. Dunn, Isogeometric collocation methods for cosserat rods and rod structures, Comput. Methods Appl. Mech. Engrg. 316 (2017) 100–122.

[25] Ashkan Almasi, Tae-Yeon Kim, Tod A. Laursen, Jeong-Hoon Song, A strong form meshfree collocation method for frictional contact on a rigid obstacle, Comput. Methods Appl. Mech. Engrg. 357 (2019) 112597.

[26] Yunhua Luo, Ulrich Häussler-Combe, A generalized finite-difference method based on minimizing global residual, Comput. Methods Appl. Mech. Engrg. 191 (13–14) (2002) 1421–1438.

[27] ABAQUS documentation, 2011, Dassault systèmes. Providence, RI, USA.

[28] Tae Yeon Kim, John Dolbow, Tod Laursen, A mortared finite element method for frictional contact on arbitrary interfaces, Comput. Mech. 39 (3) (2007) 223–235.

[29] Sang-Ho Lee, Young-Cheol Yoon, An improved crack analysis technique by element-free Galerkin method with auxiliary supports, Internat. J. Numer. Methods Engrg. 56 (9) (2003) 1291–1314.

[30] Daniel Organ, Mark Fleming, T. Terry, Ted Belytschko, Continuous meshless approximations for nonconvex bodies by diffraction and transparency, Comput. Mech. 18 (3) (1996) 225–235.

[31] Sang-Ho Lee, Young-Cheol Yoon, Meshfree point collocation method for elasticity and crack problems, Internat. J. Numer. Methods Engrg. 61 (1) (2004) 22–48.

[32] Ted L. Anderson, Ted L. Anderson, Fracture Mechanics: Fundamentals and Applications, CRC Press, 2005.

[33] J.F. Yau, S.S. Wang, H.T. Corten, A mixed-mode crack analysis of isotropic solids using conservation laws of elasticity, J. Appl. Mech. 47 (2) (1980) 335–341.

[34] Choon Fong Shih, Robert J. Asaro, Elastic–plastic analysis of cracks on bimaterial interfaces: Part I—small scale yielding, J. Appl. Mech. 55 (2) (1988) 299–316.

[35] Sang-Ho Lee, Jeong-Hoon Song, Young-Cheol Yoon, Goangseup Zi, Ted Belytschko, Combined extended and superimposed finite element method for cracks, Internat. J. Numer. Methods Engrg. 59 (8) (2004) 1119–1136.

[36] John Dolbow, Nicolas Moës, Ted Belytschko, An extended finite element method for modeling crack growth with frictional contact, Comput. Methods Appl. Mech. Engrg. 190 (51–52) (2001) 6825–6846.

[37] Fushen Liu, Ronaldo I. Borja, A contact algorithm for frictional crack propagation with the extended finite element method, Internat. J. Numer. Methods Engrg. 76 (10) (2008) 1489–1512.

[38] Chandrasekhar Annavarapu, Martin Hautefeuille, John E. Dolbow, A nitsche stabilized finite element method for frictional sliding on embedded interfaces. Part I: Single interface, Comput. Methods Appl. Mech. Engrg. 268 (2014) 417–436.

[39] Fan Fei, Jinhyun Choo, A phase-field method for modeling cracks with frictional contact, Internat. J. Numer. Methods Engrg. 121 (4) (2020) 740–762.

[40] Ashkan Almasi, Tae-Yeon Kim, Jeong-Hoon Song, Strong form meshfree collocation method for frictional contact between a rigid pile and an elastic foundation, Eng. Comput. (2022) http://dx.doi.org/10.1007/s00366-022-01673-y.

[41] Yao Fu, John G. Michopoulos, Jeong-Hoon Song, Bridging the multi phase-field and molecular dynamics models for the solidification of nano-crystals, J. Comput. Sci. 20 (2017) 187–197.

[42] Young-Cheol Yoon, Peter Schaefferkoetter, Timon Rabczuk, Jeong-Hoon Song, New strong formulation for material nonlinear problems based on the particle difference method, Eng. Anal. Bound. Elem. 98 (2019) 310–327.